# 24th Electromagnetic Induction Workshop

## 13-20 August 2018, Helsingør Denmark

**www.emiw2018.org**

# Abstracts Session 1

## SESSIONS DESCRIPTION

### Session 1. Instrumentation, sources and data processing

This session solicits contributions on EM data processing, source field analysis, instrumentation, and field practice. We welcome contributions on all aspects of data processing, including theory and practical applications. Development and application of time lapse observations (monitoring) of transfer functions and other parameters as well as new approaches to estimation of transfer functions and their uncertainty can be presented here. We also solicit studies on source fields, whether controlled or uncontrolled. This includes characterization of external source spatial structure and temporal variability, novel (distributed) transmitter configurations, and effects of finite spatial-scale sources (natural and anthropogenic) on transfer functions. Contributions on new instrumentation and field practice and related methodological developments are also appropriate for this session. Studies of sensor fidelity either by noise level analysis or by field comparison with other sensors are appropriate. Sensors can include ohmic or capacitively coupled electrodes, magnetometers, and any other instruments whose inter-comparison with EM data demonstrates new insights.

***Conveners: Pierre Wawrzyniak, Karl Kappler, Maxim Smirnov***

# A Compact Ocean Bottom ElectroMagnetic Field Receiver& Seismometer

Kai Chen[1], Li Zhou[2], Ming Deng[3], Zhongliang Wu[4]and Xianhu Luo[5]
1 China University of Geosciences (Beijing), ck@cugb.edu.cn
2 China University of Geosciences (Beijing), zhouli100083@163.com
3 China University of Geosciences (Beijing), dengming@cugb.edu.cn
4 Guangzhou Marine Geological Survey, 52936891@qq.com
5 Guangzhou Marine Geological Survey, Luoxh@163.com

**SUMMARY**

Marine electromagnetic (EM) and seismic method joint inversion and interpretations were used for offshore gas hydrate and petroleum exploration, which are producing better estimates of lithology and fluids, including de-risking of low gas saturations. Joint inversion and interpretations are wide range used, but joint data acquisition is not popular. Current marine EM data acquisition may dependent on ocean bottom electromagnetic receiver (OBEM), and ocean bottom seismometer were used to offshore seismic exploration. Joint simultaneously data acquisition will decrease cost and improve the efficient. While many conventional independent receivers are employed for offshore data acquisition, they have deficiencies, such as large size, high cost, position error and low operational efficiency. To address these limitations, we developed a compact ocean bottom electromagnetic filed receiver& ocean bottom seismometer (OBEMS). Base on the exist ocean bottom E-filed receiver (OBE) specifications, including low noise levels, low power consumption, and low clock-drift error, integrated three axis omnidirectional geophone for seismic sensor, and assemble an Ultra short base line (USBL) responder for position, improved position accuracy, the operational efficiency, and reduced the field data acquisition cost. The resulting OBEMS is comprised of a compact nylon frame, two 17-in glass sphere, logging system, geophone, batteries, recovery beacon, release mechanism, USBL responder, transducer, electrode, red flag, and anchor. It has a noise level of 0.1 nV/m/rt (Hz) at 1 Hz, and it provides 30 days of battery lifetime. It support WiFi interface to configure data acquisition parameter and data download. Offshore acquisition was performed to evaluate the OBEMS field performance during an offshore gas hydrate experiment. The results showed that the receiver effectively functioned throughout the operation and offshore data acquisition. OBEMS was thus verified as providing a low cost, compact size, and high operational efficiency for joint simultaneous data acquisition. And it designed for update future induction coil and hydro phone for fully integrated all-in-one receiver.

**Keywords:** Marine electromagnetic, Ocean bottom ElectroMagnetic receiver, ocean bottom seismometer, joint data acquisition

# A new apparent resistivity for land-based cotrolled source electromagnetic method

Xiangyu Huang1,Jingtian Tang[1], Zhengyong Ren[1],yiyuan Zhong,[1] Ziqiang Zhu[1]
[1]School of Geosciences and Info-Physics, Central South University, 410083, Changsha, China,
huangfucsu@csu.edu.cn

**SUMMARY**

Apparent resistivity can be used for quality control of raw data ,and provide useful ,stable real-time interpretation. The most common definition is the Ratio of the magnetic and electric field in the csamt method, which is applied only in far zone. Another useful definition utilizing single component is based on the projection of the electromagnetic field data to the response of electric dipole on homogeneous half-space. However it result in the nonlinear equation which need be solved by the optimization method, and sometimes the solution isn't unique. Based on the analytical solution on homogeneous half-space,we present a new fast apparent imaging algorithm for land-based controlled source electromagnetic method,and derive a new formula to get a single apparent resistivity by combining the electric and magnetic field without far-field approximation. This results in a quartic equation with one unknown quantity which is easily solved by analytical solution ,and can obtain fast estimation of apparent resistivity for every frequency and offset ,and also gives a new perspective on electromagnetic souding. We presented numerical results for 1D and 3D model.The curves of apparent resistivity proposed agree well with the cagniard apparent resistivity in far zone,but it can reflect the depth of subsurface resistive or conductive layer in the transition zone.

**Keywords:** apparent resistivity;csem; transition;zone.far zone;

Abstract, 24th EM Induction Workshop, Helsingør, Denmark, August 12-19, 2018

---

# A new open source library for MT robust processing

WAWRZYNIAK Pierre p.wawrzyniak@brgm.fr
SMAI Farid f.smai@brgm.fr
COPPO Nicolas n.coppo@brgm.fr
DARNET Mathieu m.darnet@brgm.fr
BRETAUDEAU François f.bretaudeau@brgm.fr
All at Bureau des Recherches Géologiques et Minières, 3 av., Claude Guillemin, BP 36009, 45060 Orléans Cedex2, France

---

A new open source Python library, named Razorback, is designed to handle, manipulate and combine time series of synchronous data. This modular library allows users to plug in data prefilters and includes both M-estimator and bounded influence techniques, as well as a two-stage multiple remote reference. We performed validation on a real data set by comparing the results with those of an existing code.

The developed library allows for the design of complex and specific processing procedures. As examples, we performed i) continuous time lapse processing and ii) processing of one site in a peri-urban context. In the latter case, we have tested all possible combinations of remote reference stations in an MT array, using the two-stage remote reference approach. Our phase tensor analysis shows that the bounded influence outperforms the M-estimator in reducing the impacts of man-made electromagnetic noise on magnetotelluric soundings. The Razorback open source library initiate a collaborative platform for MT users.

**Keywords:** MT robust processing, phase tensor, time lapse, remote reference, open source library

# Current and voltage source induced polarization responses: a general consideration

N. Kozhevnikov[1,2], and E. Antonov[1]
[1]Institute of Petroleum Geology and Geophysics, SB RAS, kozhevnikovno@ipgg.sbras.ru
[2]Novosibirsk State University, kno48@yandex.ru

**SUMMARY**

There are several models accounting for the induced polarization (IP) phenomenon in terms of complex frequency dependent conductivity $\sigma$ or resistivity $\rho = 1/\sigma$. The most frequently used model is the Cole-Cole model which, when represented in terms of resistivity, is also known as the Pelton model. Parameters of the Cole-Cole model are DC conductivity $\sigma_0$ (or resistivity $\rho_0$), chargeability $m$, time constant $\tau$ and exponent $c$. It is believed that these parameters determine the induced polarization response of geological materials. For quantitative interpretation of IP data two methods are used. The first one is inversion by searching the Cole-Cole parameters ($\rho_0$ or $\sigma_0$, $m$, $\tau$, $c$) that provide the best fit of the measured response. The second method, referred to as Debye decomposition, gives the relaxation time distribution.

However, along with the Cole-Cole parameters, IP response also depends on whether the current or voltage source is used in field IP survey or in laboratory studies. We illustrate this with the example of time domain IP response using the Cole-Cole IP relaxation model.

Excitation of IP transients by a current source has found a wide application in induced polarization surveys and, directly or indirectly, in the theory of the IP method. Typically, rectangular current pulses are injected into the earth via grounding electrodes and decaying induced polarization voltage is measured during the pauses between pulses. In this case, only the secondary field is recorded in the absence of the primary one, which is an important advantage of this method. On the other hand, since the current injected into the ground is fully controlled by the source, this method does not allow studying induced polarization by measuring the current in the transmitter line or associated magnetic field. Debye decomposition of IP voltage response to current pulses results in the relaxation time distribution straightforwardly predicted by the Cole-Cole resistivity model.

When energizing the earth or a rock sample with voltage pulses, the measured quantity is the transient induced polarization current. Considering the IP transient current suggests some specific features of this method. First, the time constant of IP current decay does not equal $\tau$ of the Cole-Cole resistivity model. In the simplest case of $c$=1 (Debye relaxation) it is given by $\tau$ (1 – $m$). Sometimes this difference between relaxation spectra is attributed to the difference between resistivity and conductivity formulations of Cole-Cole model. However, both these formulations are equivalent. In fact, the difference is due to whether a current or voltage source is used to produce an IP response.

Excitation of IP current transients using a voltage source allows induced polarization studies to be done by recording the transmitter line current, the associated magnetic field, or its rate of change. However, the decay of current in a grounded transmitter line depends not only on the induced polarization of the earth but also on the polarization of the grounding electrodes. This problem does not occur when IP transients are excited inductively. A grounded transmitter line is a mixed-type source; hence, for a purely inductive excitation of induced polarization transients, one should better use an ungrounded loop which is coupled to the earth solely by electromagnetic induction.

Using an ungrounded loop or coil as the receiver removes also the problem caused by the polarization of measuring electrodes. Additional advantages are that the inductive source response is insensitive to transverse anisotropy and enables studying polarizable targets under non-conductive strata.

It is straightforward to show that corresponding differences are observed also in frequency domain IP studies.

**Keywords:** Induced polarization, Cole-Cole model, inductive source IP response

# Development of the MTPy software package for magnetotelluric data analysis

A. Kirkby[1], J. Peacock[2], F. Zhang[3], R. Hassan[4] and J. Duan[5]
[1]Geoscience Australia, Alison.Kirkby@ga.gov.au
[2]United States Geological Survey, jpeacock@usgs.gov
[3]Geoscience Australia, Fei.Zhang@ga.gov.au
[4]Geoscience Australia, Rakib.Hassan@ga.gov.au
[4]Geoscience Australia, Jingming.Duan@ga.gov.au

## SUMMARY

The MTPy Python library is open source software that aims to facilitate processing, analysis, modelling, and inversion of magnetotelluric (MT) data. Until recently, MTpy has contained bugs and gaps in both functionality and documentation, which have limited its use to date. We are developing MTPy to rectify these problems and expand functionality. Key improvements include adding new functions and classes to the modules that handle ModEM inputs and outputs, improving data and model visualization tools, refactoring the code to improve maintainability, quality, and consistency, and developing documentation.

**Keywords:** magnetotellurics, python, software, analysis, processing

## INTRODUCTION

The magnetotelluric (MT) method is increasingly being applied to a wide variety of geoscience problems, as inversion tools and compute facilities become more sophisticated. However, the software available for MT data analysis and interpretation is still very limited in comparison to other geophysical methods such as gravity, magnetics, and seismic.

MTpy is an open source software package that has been developed to assist with MT data processing, analysis, modelling, visualization and interpretation. It was initiated at the University of Adelaide in 2013 as a means to store and share Python code amongst the MT community (Krieger and Peacock, 2014).

Written in the Python programming language, MTpy contains modules to carry out much of the processing and analysis that needs to be applied to MT data, working with the industry standard EDI file format amongst other formats. MTPy also contains modules to create inputs to, and visualize outputs from the Occam 1D and 2D (Constable et al., 1987, deGroot-Hedlin and Constable, 1990), and ModEM 3D (Egbert and Kelbert, 2012, Kelbert et al., 2014) inversion codes. However, until recently, much of the code has lacked internal unit tests, and contained bugs and gaps in functionality. These factors have limited its use in the wider MT community to date.

Geoscience Australia in collaboration with developers at the University of Adelaide and the United States Geological Survey continue to develop MTpy to improve its functionality and provide increased user support. The aim is to make the software toolkit easier to use and thus facilitate the use of MT in the wider geophysics community.

## FUNCTIONALITY DEVELOPMENT

MTpy is structured around key steps in working with MT data, namely processing, analysis, modelling, and imaging. These sub-packages are based upon the core modules, which deal with reading and writing impedance tensor data from industry standard formats such as EDI (Figure 1, Krieger and Peacock, 2014).

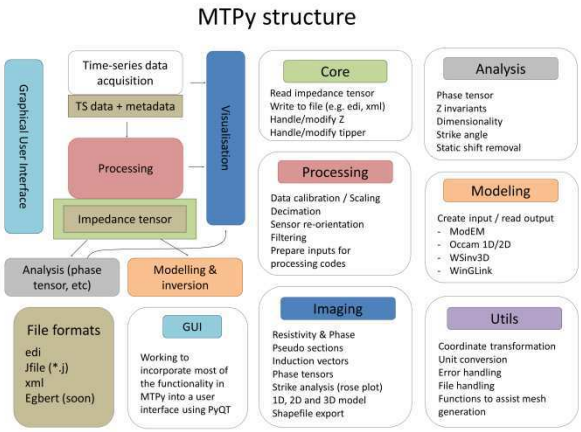


**Figure 1.** MTPy package structure, modified after Krieger and Peacock (2014).

The processing modules are designed to facilitate working with time series data and generating inputs

for existing processing codes, for example, the processing code BIRRP (Chave et al 1987, Chave and Thomson, 2004).

The analysis modules include phase tensor and dimensionality analysis, calculation of impedance tensor invariants, and calculation and removal of distortion. Recent developments include addition of functions to calculate and visualize depth of investigation using the Niblett-Bostick transform (Jones, 1983).

A number of changes have been added to the modelling modules in MTPy. These modules cover creation of inputs and analysis of outputs for many of the widely used modelling codes used in the MT community. Improvements to the modelling modules over the last 12 months have focused mainly on creating inputs for and viewing outputs from the ModEM code (Egbert and Kelbert, 2012, Kelbert et al, 2014).

Recent developments to the ModEM modules in MTpy include the addition of modules to allow topography and bathymetry to be added to models, and to allow reading and writing of models to and from GOCAD™ sgrid format. GOCAD™ is a software package developed by Paradigm for 3D spatial analysis and geological modelling, and will allow for more detailed analysis of resistivity models produced by ModEM. We have also made developments to the handling of projections in ModEM, to facilitate the creation of large models that cross UTM zones. Finally, updates have been made to the visualization modules, allowing visualization of input data and modelled responses as plots showing resistivity and phase as a function of period, and as phase tensor maps. In addition, the modules allow plotting of resistivity models as depth slices and cross sections.

As well as adding to the functionality contained in MTpy, we are working to apply software engineering best practices and techniques to improve software quality and usability. In addition, a GUI is being developed (Figure 1) to assist with the use of all MTpy modules. Our aim is to make MTpy a comprehensive toolkit that can be easily installed and used by the wider geophysics community.

## CONCLUSIONS

The MTpy Python library was created to assist with many aspects of MT data processing, analysis and modelling. Geoscience Australia in collaboration with developers at the University of Adelaide and the United States Geological Survey continues the development to improve functionality, remove duplication, and facilitate its use. Key developments include improvements to the processing modules, addition of functions to calculate and visualise penetration depth, and improvement to the modelling modules to assist with creation of input files, and visualisation and analysis of outputs. A GUI is also being developed to help with the easy use of the functions contained within MTpy. For more updated details please visit the open source code repository: https://github.com/MTgeophysics/mtpy.

## REFERENCES

Chave A.D., Thompson DJ and Ander, M.E. (1987) On the robust estimation of power spectra, coherences and transfer functions. Journal of Geophysical Research 92: 633–648.

Chave, A.D., and Thomson, D.J. (2004) Bounded influence magnetotelluric response function estimation. Geophysical Journal International 157: 988–1006.

Constable, S. C., R. L. Parker, and C. G. Constable, (1987) Occam's inversion — A practical algorithm for generating smooth models from electromagnetic sounding data, Geophysics, 52: 289–300.

deGroot-Hedlin, C., and S. Constable (1990) Occam's inversion to generate smooth two-dimensional models from magnetotelluric data, Geophysics, 55 (12), 1613–1624.

Egbert, G. D. and Kelbert, A. (2012) Computational recipes for electromagnetic inverse problems. Geophysical Journal International, 189 (1): 251-267.

Jones, A.G. (1983) On the equivalence of the "Niblett" and "Bostick" transformations in the magnetotelluric method. Journal of Geophysics 53: 72-73.

Kelbert, A., Meqbel, N., Egbert, G. D., and Tandon, K. (2014) ModEM: a modular system for inversion of electromagnetic geophysical data. Computers & Geosciences, 66: 40-53.

Krieger, L. and Peacock, J. (2014) MTPy: A Python toolbox for magnetotellurics. Computers and Geosciences, v. 72, pp. 167-175.

# Differential Magnetometer Measurements of Geomagnetically Induced Currents in the UK Power Grid

J. Huebert[1], C. Beggan[1], T. Martyn[1], A. Swan[1], T. Taylor[1], C. Turbitt[1] and A. Thomson[1]
[1]British Geological Survey, Edinburgh, UK,
juliane.huebert@bgs.ac.uk

## SUMMARY

Extreme events of space weather can have severe effects on satellites and other technology in orbit, but also pose potential risk to ground-based infrastructure like power lines, railways and gas pipe lines through the induction of geomagnetically induced currents (GICs). Modelling GICs requires knowledge about the source magnetic field and the conductivity structure of the Earth to calculate electric fields during enhanced geomagnetic activity. The electric field in combination with detailed information about the network topology enable the derivation of GICs in power lines. Directly monitoring GICs in power grid substations is possible with a Hall probe, but scarcely realised. In the UK, data from only four such stations located in Scotland is available at the moment. Therefore we will deploy the differential magnetometer method (DMM) to measure GICs across the whole UK power grid, specifically in high voltage network segments that appear as hotspots during electric field calculations for historic geomagnetic storms due to their location within the network (mainly the distances between transformer substations) and the underlying conductivity and coastal effects in the British Isles.

The setup of the DMM includes the installation of two fluxgate magnetometers, one directly under a power line affected by GICs, and one as a remote site further away. The difference in recordings of the magnetic field in both instruments allows for the calculation of GICs in the respective power line segment. The recorded data are transferred back in real-time to the geomagnetic data centre in Edinburgh and compared to the predicted GICs. The installation of DMM instrumentation at around 12 sites in the UK is anticipated to validate theoretical modelling of GICs and improve the understanding of effects and hazards on the power grid.

**Keywords:** Space Weather, GIC, Differential Magnetometers

# Effect of conductive ground on current transients in a closed loop conductor used for testing TEM measuring systems

Nikolay Kozhevnikov, Evgeny Antonov
Institute of petroleum geology and geophysics SB RAS, KozhevnikovNO@ipgg.sbras.ru

**SUMMARY**

In recent years, transient current response of a closed wire loop is increasingly used for testing TEM systems. If the ground is resistive, it does not affect the transient current in the loop conductor. However, in general the ground effect must be taken into account. We describe the first version of the computer program for calculating current transients in a loop conductor with regard to the effect of horizontally layered conductive ground. We also give and discuss an example of the calculations using this program.

**Keywords:** TEM system, loop conductor, conductive ground

## Introduction

A wire loop conductor located on the ground has been used to test and calibrate airborne and ground TEM systems (Davis and Macnae 2008; Yin and Hodges 2009; Kozhevnikov 2012). It is important that, when using such a large conductor, the intrinsic TEM system response is the same as in the case of search for and studies of natural targets. This ensures the manifestation of the limitations that may not be identified and, accordingly, evaluated in the laboratory.

## Testing procedure

A measurement scheme for testing a TEM system is shown in Figure 1. In addition to the transmitter (1) and the receiver (3) loops, a loop conductor (2) is laid out on the ground. Its terminals are connected to a circuit with impedance $Z$, which, in general, can be complex and frequency dependent. In the simplest and practically most interesting case, this is a resistor with resistance $R$.

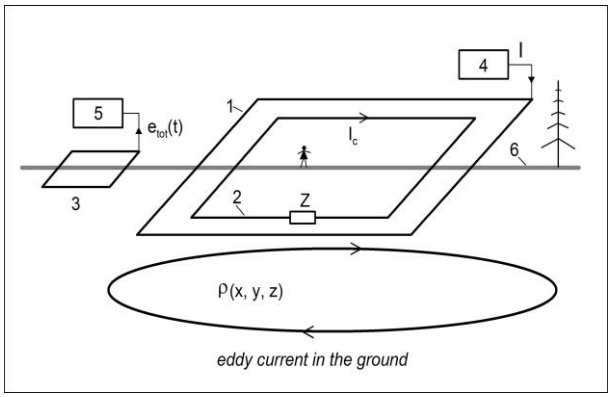


**Figure 1.** Testing a TEM system: 1, transmitter loop; 2, loop conductor connected to a circuit with impedance $Z$; 3, receiver loop; 4, transmitter unit; 5, receiver unit.

Each loop in Figure 1 is inductively coupled to the others. This coupling is determined by the mutual induction between: the transmitter loop and the loop conductor ($M_{12}$), the conductor and the receiving loop ($M_{23}$), the transmitter and receiving loops ($M_{13}$).

Suppose that transmitter and receiver loops, as well as the loop conductor, are located on the surface of a non-conducting ground. In this case, the EMF induced in the receiver loop by the current in the loop conductor is determined by the TEM array geometry and parameters of the loop conductor.

When the current $I$ in the transmitter loop is turned off, a vortex electric field is induced, under the action of which an eddy current $I_c$ appears in the loop conductor. This current decays exponentially inducing EMF $e_1(t)$ in the receiver loop. At times greater than transmitter loop current turn-off ($t_{off}$), $e_1$ decays exponentially:

$$e_1(t) = \frac{I_1}{t_{off}} \frac{M_{12} M_{23}}{L} \left(1 - e^{-t_{off}/t}\right) e^{-t/\tau}. \qquad (1)$$

Here, $\tau = L/R_m$ is a time constant of the loop conductor, $L$ is its inductance; $R_m = R_c + R$, where $R_c$ is the resistance of the loop conductor.

Actually, the ground is conductive, so after the current in the transmitter loop is turned-off, transient eddy currents flow in the ground. These currents induce an EMF in the loop conductor; therefore, its transient response depends on the electrical properties of the ground. We denote the EMF induced in the receiver loop by the eddy currents in the earth as $e_g(t)$. EMF induced in the receiver loop by the transient current in the loop conductor, taking into account the effect that the ground has on this transient current, we denote as $e_2(t)$. The total EMF, $e_{tot}(t)$, induced in the receiver

loop can be represented as $e_{tot}(t) = e_g(t) + e_2(t)$. In the case of resistive ground or small TEM arrays, when eddy currents in the loop conductor and in the ground are not coupled, testing is simple. First, with an open loop conductor, the EMF $e_g(t)$ is measured. Then a resistor is connected across the conductor loop and the total transient response $e_{tot}(t)$ is measured. To find $e_2(t)$, the ground transient response is subtracted from the total one:

$e_2(t) = e_{tot}(t) - e_g(t)$.

Finally, $e_2(t)$ is compared with $e_1(t)$ calculated using equation 1. It is obvious that the smaller difference between these responses, the better the measuring TEM system.

**Effect of the conductive ground**

As mentioned above, EMF acting on the loop conductor is created not only due to a transmitter current turn-off, but also by the eddy currents flowing in the ground. Therefore, in order to calculate current $I_c(t)$ in the loop conductor, one has first to calculate EMF $e_{cg}(t)$, induced in the loop conductor by eddy currents in the ground, and then to convolve $e_{cg}(t)$ with current impulse response $i(t)$ of the loop conductor: $I_c(t) = e_{cg}(t) * i(t)$.

The current impulse response describes the current exited in the loop conductor under the action of a very short EMF pulse with an area of 1V·s. For a wire loop connected to a resistor $i(t)$ = (1V·s / L) exp $(-t / \tau)$, where $\tau = L/R_m$.

Previously, calculations of $I_c(t)$ with allowance made for the ground effect were carried out only for circular coaxial loops located on the surface of a homogeneous conductive ground (Kozhevnikov 2012). Recently, E. Antonov wrote a FORTRAN code enabling calculation of $I_c(t)$ and $e_2(t)$ for square loops on the surface of a horizontally layered conductive ground.

The program performs the following operations:

Calculation of the EMF $e_{cg}(t)$, acting on the square loop conductor during and after the linear current turn-off in the square transmitter loop, with allowance made for the effect of eddy currents in the ground. Conductor can be located both inside and outside the transmitter loop, or coincide with it.

The current $I_c$ flowing in the loop conductor is found by the convolution of $e_{cg}(t)$ with the current impulse response $i(t)$ of the loop conductor.

Calculation of the derivative $dI_c/dt$ needed to calculate $e_2(t)$ induced in the receiver loop due to the current decay in the loop conductor:

$$e_2(t) = -M_{23}\frac{dI_c}{dt}.$$

Figure 2 shows calculation results for a TEM array with 100m by 100m coincident transmitter and receiving square loops located on the surface of a two-layer ground ($\rho_1$ = 400 Ω·m, $h_1$ = 120m, $\rho_2$ = 25 Ω·m). A square loop conductor (50m by 50m in size) of insulated copper wire is located coaxially with the transmitter and receiver loops. The loop conductor is short-circuited ($R$=0); therewith the decay time constant of the transient current is 0.8 ms. The transmitter loop current of 1A was assumed to turn off linearly in a time of 10 μs.

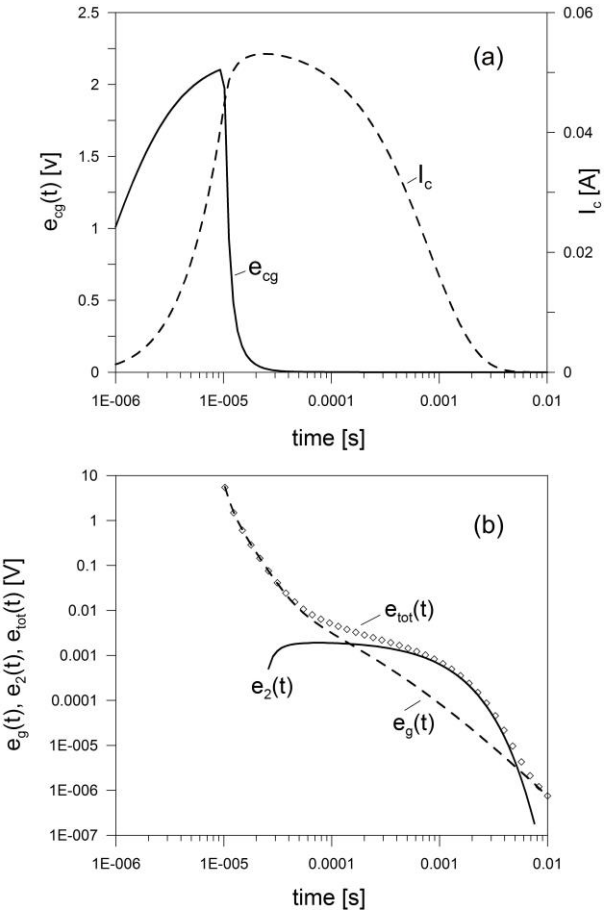


**Figure 2.** An example of calculation: (a) EMF $e_{cg}(t)$, and current $I_c$ in the loop conductor; (b) EMF $e_g(t)$ induced in the receiver loop by the eddy currents in the ground, EMF $e_2(t)$ induced in the receiver loop due to decay of $I_c$, and the total EMF $e_{tot}(t)$.

As shows Figure 2a, EMF $e_{cg}(t)$ increases during the transmitter current turn-off and decreases after the current is turned off. Under the action of this EMF, a current $I_c$ appears in the loop conductor. This current's change induces EMF $e_2(t)$ in the receiver loop. This EMF is summed with the EMF $e_g(t)$ induced in the receiver loop due to decay of

the eddy currents in the ground (Figure 2b). The graph shown in Figure 2 by crosses represents the total EMF $e_9(t) + e_2(t)$ induced in the receiver loop due to decay of currents both in the loop conductor and in the conductive ground. The modeled responses of Figure 2 have very much in common with transient responses measured during field survey (Kozhevnikov 2012).

Considering the utility of the above approach to testing TEM systems, one may ask a question: why do we need a loop conductor? After all, if we know electrical structure of the ground, we can simply compare the measured and model TEM responses of the ground. In recent years, such an approach based on measuring TEM responses over reference sites has been used to test and calibrate ground and airborne TEM systems (Foged et al. 2013; Lavoue et al. 2010).

However, the experience of TEM surveys shows that sometimes it is difficult, if possible, to understand whether anomalous TEM response is due to the geology or to the intrinsic transient response of the TEM system. Most often, this problem arises when using small TEM arrays (Sharlov et al. 2017).

Just in such cases, using a loop conductor makes it possible, even under complicated conditions, to design and carry out a controlled experiment. That allows one to understand in what time range and with what error the measured TEM response reflects geology, and when the intrinsic response of the TEM system does predominate.

## Conclusions

A large wire loop connected to the resistor allows testing TEM systems.

If the ground is weakly conducting, it does not affect the loop conductor's contribution to the TEM response. In this case it is sufficient to measure the EMFs induced in the receiver loop at open and closed loop conductor, then find the difference between these EMFs and compare it with the EMF calculated using 1.

In the case of conductive ground, transient current in the loop conductor is affected by eddy currents in the ground. To account for this effect, a FORTRAN program is written. Transient responses calculated using this program have the same features as those measured in the field.

## Acknowledgments

The research was carried out with the financial support of RFBR grant 18-05-00363 "Mathematical modeling and experimental study of induction current transients in a closed horizontal loop with regard to the effect of the conductive earth".

## References

Davis AC, Macnae J (2008) Quantifying AEM system characteristics using a ground loop. Geophysics 73: F179 – F188. doi:10.1190/1.2943189

Foged N, Auken E, Christiansen AV, Sørensen KI (2013) Test-site calibration and validation of airborne and ground-based TEM systems. Geophysics 78: E95–E106 doi:10.1190/geo2012-0244.1

Kozhevnikov NO (2012) Testing TEM system using a large horizontal loop conductor. Russian Geology and Geophysics 53: 1243 – 1251. doi:10.1016/j.rgg.2012.09.010

Lavoue F, Van Der Kruk J, Rings J, Andre F, Moghadas D, Huisman JA, Lambot S, Weihermüller L, Vanderborght J, Vereecken H (2010) Electromagnetic induction calibration using apparent electrical conductivity modelling based on electrical resistivity tomography. Near Surface Geophysics 8: 553–561. doi: 10.3997/1873-0604.2010037

Sharlov MV, Kozhevnikov NO, Sharlov RV (2017) Lake Baikal – A Unique Site for Testing and Calibration of Near-surface TEM Systems. Near Surface Geoscience 3-7 September 2017, Malmö, Sweden. 5 pp. doi:10.3997/2214-4609.201702038

Yin C, Hodges G (2009) Wire-loop surface conductor for airborne EM system testing. Geophysics 74: F1-F8. doi:10.1190/1.3008055

# EM-ACROSS experiment at Kusatsu-Shirane volcano

K.H. Tseng[1], Y. Ogawa[2], T. Kunitomo[3], M. Fukai[4], E. A. Bertrand[5], Y. Kinoshita[6] and T. Minami[7]
[1]Tokyo Institute of Technology, tseng.k.aa@m.titech.ac.jp
[2] Tokyo Institute of Technology, oga@ksvo.titech.ac.jp
[3]Nagoya University, kunitomo@seis.nagoya-u.ac.jp
[4] Tokyo Institute of Technology, fukai.m.ab@m.titech.ac.jp
[5]GNS Science, t.bertrand@gns.cri.nz
[6] Tokyo Institute of Technology, kinoshita.y.ah@m.titech.ac.jp
[7]University of Tokyo, tminami@eri.u-tokyo.ac.jp

**SUMMARY**

The Accurately Controlled, Routinely Operated, Signal System (ACROSS) is a system which combines at last one controlled source transmitter with one signal receiver for investigating the subterranean space. The accurately controlled signal lets us be able to discriminate that from other background signal in data analysis. The routinely operated signal provides a robust anti-noise ability while stacking the recorded signal in processing. The EM-ACROSS is one kind of the above- mentioned system that using electromagnetic wave for the transmitted signal.

In this study, we designed a signal transmitter for injecting the current into two pairs of the grounded electrode arrays. The signal is a superposition of harmonics which generated with arbitrary phase shift and same amplitude. The transmitter is continuously synchronized with a 10M Hz GPS signal for ensuring the accurate control. A GPS synchronized signal logger is connected with the transmitter for the subsequent signal analysis. We use MTU-5 series magnetotelluric receiver from Phoenix- Geophysics to be our signal receiver. At Kusatsu-Shirane volcano, we set 9 sites for MT stations which are 3.6 km to 5.6 km far from the transmitter. Each MT receiver records at last 10 hours data for the signal from both current dipoles.

The integrality and stability of transmitted signal is confirmed by analyzing the logged data from transmitter. In the processing of received signal analysis, we use stacking method which divides the entire time series into minor frames then stacks each frame in frequency domain after tacking the Fast Fourier's Transform. This method provides the high signal-to-noise ratio (SNR) while we do a large enough number of stacking, which associate with the data quality, ambient noise level, and the strength of controlled source. We compare different numbers of stacking for the data from same MT station record and confirm that the sufficient stacking is one of the focal point to get high SNR.

The result of received signal analysis presents that the anti-noise ability of EM-ACROSS method is distinguished at higher specific frequencies, particularly in one of our station, which is a very noisy area with continuous and stable anthropogenic noise. Therefore, we are able to consider more location for the MT station with this system while we are planning the investigation. With the EM-ACROSS survey, we can use the value of injected current, electric and magnetic fields from our specific frequencies to calculate the modeling parameters as from conventional MT survey. And this system provides more ability while we aim a subterranean target in noisy area.

**Keywords:** magnetotelluric, geophysical prospecting, geophysical techniques, controlled-source electromagnetics

# Features of audiomagnetotellurics daytime signal in dead band in Chukotka (Russian Far East)

E.Ermolin[1], O.Ingerov[2], A.A.Yankilevich[3], N.N.Pokrovskaya[3], T.V.Davytkina[3], V.Melnikov[1]
[1] «GM-Service» LTD, e.ermolin.gms.@gmail.com
[2] «Phoenix Geophysics» LTD, olexandr_ingerov@yahoo.ca
[3] «Saint-Petersburg Mining University», yankilevich@mail.ru

## SUMMARY

In this paper we analyze the amplitude spectra of the audiomagnetotelluric (AMT) natural-source signal. Special attention is given to the signal in the frequency range from 1 kHz to 5 kHz known as "dead band". We study the measurements of the base sites that were used during summer fieldwork in 2013, 2014 and 2017 in Chukotka Region (Russian Far East). The area is located above the Arctic Circle. As it has been described by previous researchers, the stable signal in the dead band can be acquired only at nighttime. We would like to point out that in the daytime the local maximum at 2.4 kHz frequency is observed within the dead band in Chukotka. The 2.2 kHz and 2.6 kHz frequencies can be reconstructed by using more than 3 hours of daytime data acquisition. These frequencies can be used as the ranging marks. These ranging marks sometimes allow to reconstruct the AMT curve by using the relationship between the amplitude and phase. We present a proposal for improving data quality in the dead band during the daytime.

**Keywords:** Magnetotellurics, magetovariational profiling, EM monitoring, amplitude spectra, dead band

## INTRODUCTION

Magnetotellurics sounding (MT) and magnetovariational profiling (MVP) methods (Berdichevskiy and Dmitriev 2008) are realized as the result of measuring 5 components of the natural alternative electromagnetic field of the Earth. This technique is a reliable instrument for performing a large number of exploration tasks. For investigation at smaller depths (less than 2 km), the high-frequency modification of magnetotelluric method - AMT (audiomagnetotellurics) is applied. In the AMT modification, the frequency range from 10 (50) kHz to 1 Hz is used depending on the modification of magnetic sensors. It is considered that the source of the field in AMT is thunderstorms in equatorial regions. When this occurs, the minimum of the signal amplitude is present in the frequency range from 5 kHz to 1 kHz. The pointed range is called “dead band”. An extensive study of this problem is found in Xavier Garcia and Alan G. Jones' (2002) article. For enhancing data quality in the dead band they propose the following: 1. perform a sounding at night; 2. increase the sensitivity of magnetic sensors; 3. use more than one reference point for processing. At present, a new approach has appeared: dispersion relationship in the magnetotelluric tensor in the first stage of data processing using (Jones 2017). Unfortunately, it is hardly ever feasible to apply all the given recommendations. However, the information about the curve in dead band is very important for many exploration tasks.

We performed AMT survey for gold exploration in Chukotka (Ermolin et al 2014). The area is located above the Arctic Circle where the signal in the dead band is much weaker. Nighttime measurements were the only way to acquire adequate data in the high-frequency band. That decreased the productivity of the fieldwork significantly. Nevertheless, some measurements were carried out in the daytime in the hope of obtaining AMT curves of an adequate quality. In Jule and August, it can be done with a 50-70 % chance and in October with a 10% chance. The purpose of this investigation is to search for the features of the amplitude spectra of 5 field components (Ex, Ey, Hx, Hy, Hz). Some features will probably help to find new ways of enhancing the curve quality in the dead band.

## METHODS

We used the records of the remote reference sites in the periods of fieldwork in Chukotka: August-

October 2013; June-September 2014; July-August 2017. The natural field was registered daily for 15 hours from 12:00 to 8:00 local time. The averaged coordinates of the area are: Longitude: 170º E, Latitude: 70º N. MTU-5A receivers, AMTC-30 magnetic coils and the non-polarized lead electrode by "Phoenix-Geophysics Ltd" were used. The magnetic sensors were installed on the tripods manufactured by "AGCOS Inc". All the cables and tripods were buried in the base site. At the 24 kHz sampling frequency, 4 records in each of the second timeslot (timeslot length is 10 seconds) were used. The results of data acquisition (time-series) were divided into 30-minute intervals. SSMT2000 software was used for data processing. Local impedance estimates (Local E) were used.

### THE DATA ANALYSIS AND RESULTS

We visualized the results of data processing. The analysis has been done for: I – amplitude spectra as the function of time; II – the curves of amplitude spectra; III – amplitude at the 3 kHz and 1.5 kHz frequencies; IV – AMT curves analysis. All the data are shown for the same site.

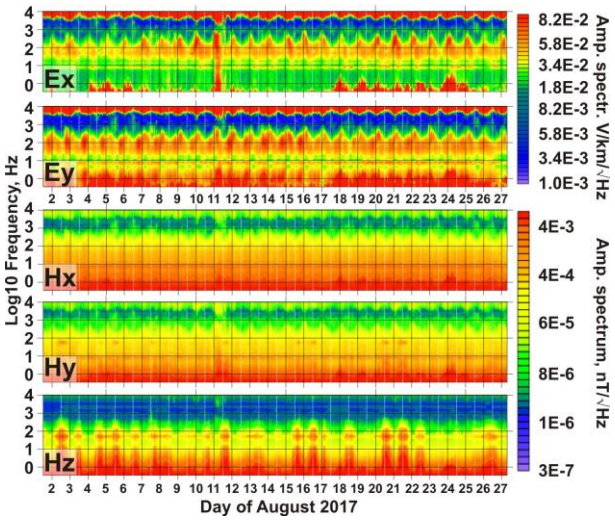


**Figure 1.** AMT Amplitude spectra in August 2017.

**I. The amplitude spectra** for 5 components as the function of time are shown in figure 1 (August 2017). In the dead band, the clear periodicity of the signal amplitude is observed which is connected with a certain time of the day. This blue-purple band of the low value in all the components at the frequency band from 6 kHz to 0.9 kHz contracts and expands over time. It gets widest (the lowest amplitude) from 12:00 to 15:00 (in the daytime) and it gets narrowest (the maximum amplitude) from 00:00 to 03:00 (at night). The 11 of August stands out in the average regularity. On this day an abnormally large amplitude spectral value is observed throughout the day. The dead band is shown more detailed in figure 2 from 8 to 13 of August in the frequency range from 10 kHz to 0.1 kHz.

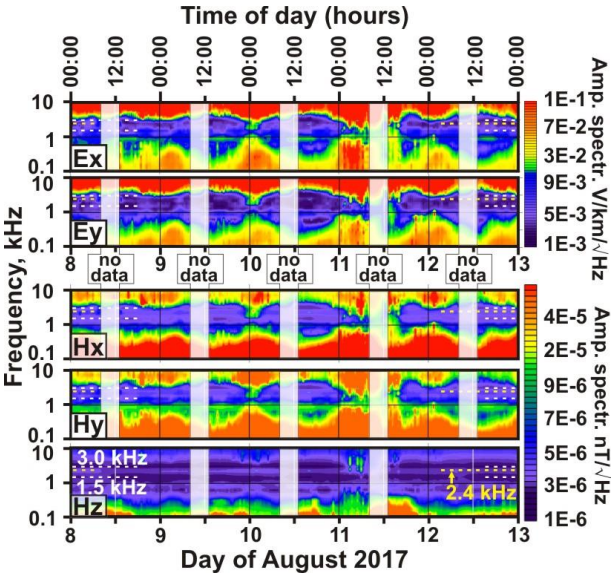


**Figure 2.** Amplitude spectra from 8 to 13 of August.

In figure 2 the general minimum of the amplitude spectra in the dead band is observed in the daytime. But at the same time, the local maximum is observed at frequency 2.4 kHz within the general minimum. This local maximum is more visible in the vertical magnetic component. Over here the two local minimums of the dead band are clearly observed: 3 kHz and 1.5 kHz. We also visualized the curves to analyze the features of amplitude spectra in the daytime more detailed.

**II. Frequency characteristics** of a 4-hour daytime record on August 8 (from 12:30 to 16:30) and a short 30-minute night record on August 9 (from 02:00 to 02:30) are shown in figure 3. These are typical spectra in the field seasons of 2013, 2014 and 2017. In figure 3 it is clearly seen that the amplitude spectra at night is higher than those in the daytime. In figure 3 on daytime spectra in the dead band, the local maximum is clearly observed at the frequencies 2.2 kHz and 2.6 kHz. This local maximum is marked by a transparent blue square in figure 3. The table in figure 3 demonstrates that the amplitude spectra of the local maximum in the dead band are higher by 85% (relative to the values of two nearby local minimums). Thus, there is a strong possibility that the AMT curve can be rebuilt at the local maximum using the daytime record. The presence of the local maximum in the dead

band can be an indicator of sufficient data quality in the daytime. Consequently, for daytime measurements it is essential to carry out an operative analysis of the amplitude spectra immediately after recording in field conditions.

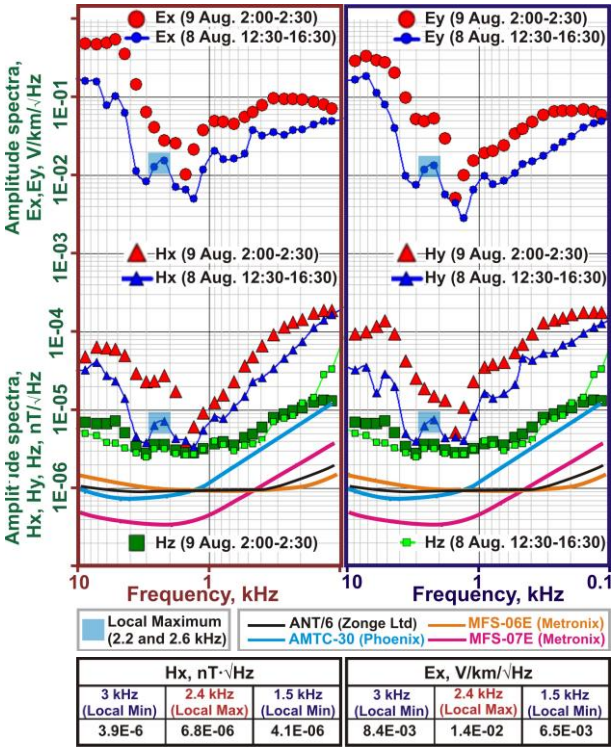


| Hx, nT·√Hz | | | Ex, V/km/√Hz | | |
|---|---|---|---|---|---|
| 3 kHz (Local Min) | 2.4 kHz (Local Max) | 1.5 kHz (Local Min) | 3 kHz (Local Min) | 2.4 kHz (Local Max) | 1.5 kHz (Local Min) |
| 3.9E-6 | 6.8E-06 | 4.1E-06 | 8.4E-03 | 1.4E-02 | 6.5E-03 |

**Figure 3.** The comparison of the amplitude spectra measured at night and in the daytime. Sensitivity characteristics of sensors are shown as lines (the manufacturer's website official data). Hx and Ex local maximum and two local minimum amplitude values in the daytime are shown in the table.

It should be noted that in the dead band the amplitude of magnetic components is lower than that of electric components (relative to 100 Hz frequency). Therefore, the noise in magnetic channels is greater than noise in electric channels. For this reason, for the dead band in the investigated area, we used the results of impedance estimates (Remote E). The comparison between the natural-signal amplitude levels and official sensitivity characteristics of the commonly used sensors are shown in figure 3. This figure illustrates that the own noises of modern magnetic sensors are significantly lower than the natural-signal amplitude in the dead band. Consequently, the dead band problem is not connected with the sensor sensitivity but in a greater degree with external noises. As a result, there is a crucial task is improve the ways of sensor installation that allows to decrease external noises.

Due to high noises in the magnetic channels, the values of apparent resistivity appear to be substantially smaller. This is what we observe in the dead band.

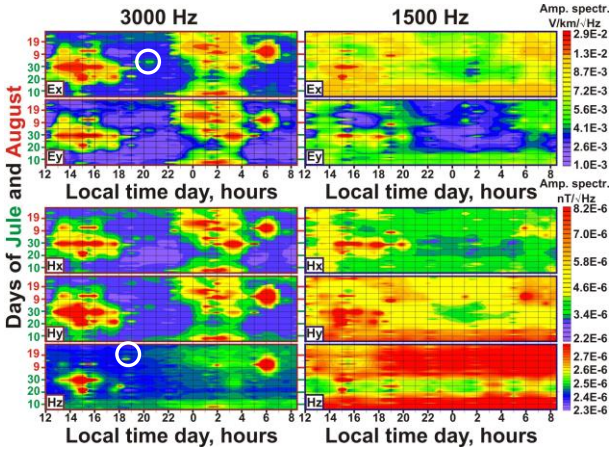


**Figure 4.** Dependence of the signal amplitude in the local time of the day from July 4 to August 26 at frequencies 1.5 kHz and 3 KHz. Local maximums are shown with white circles.

**III. The signal amplitudes at 1.5 kHz and 3 kHz** have minimum values in the dead band. For this reason, we performed a detailed analysis of these frequencies specifically. The results are shown in figure 4. At 3 kHz frequency, the signal is higher at night from 0:00 to 4:00 for all components. Also, from July 15 to August 15 the increased values are observed from 13:00 to 17:00 local time. At 1.5 kHz frequency, the signal level is higher in the daytime. At night from 22:00 to 5:00, the values are low. That is why the frequency 1.5 kHz is the most challenging problem concerning the dead band.

Single local anomalies of the increased amplitude values deserve special attention (the white circles in Figure 4). They chaotically appear throughout the day. We used the MTU-5A receivers, where at a sampling frequency of 24 kHz, in fact only 2% to 5% of the measurement time is recorded. The increase in the sampling frequency and the recording of continuous time series will probably help to measure the rarer "impulses" of the signal. It is likely that this technique will help to partially solve the problem with the data quality of AMT curves in the dead band.

**IV. The apparent resistivity curves** and impedance phase curves are shown in Figure 5 for a short daytime record (5-a), 4-hour daytime record (5-b), and 15-hour record (5-s). The remote-reference processing was applied.

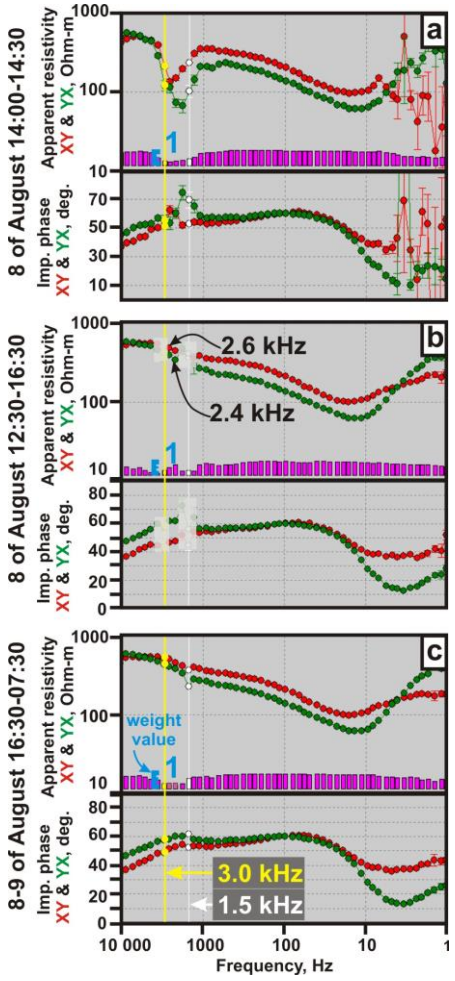


**Figure 5.** Apparent resistivity curves and impedance phases for: a 30-minute (a) and 4-hour (b) daytime record on August 8; 15-hour night record on August 8-9 (c). Chukotka region.

The curve in figure 5-a is a rejected take because the values at 11 consecutive frequencies in the dead band at the amplitude and phase deviate significantly from the real curve.

The curve in figure 5-b is of much better quality. The main feature is that the frequencies of the local maximum (2.2 kHz and 2.6 kHz) can be restored as a result of the interactive rejection of solutions with a low weight. Due to the presence of these benchmarks, we can restore the curve in the dead band. As a rule, 1-2 frequencies above and 2-3 frequencies below are removed in practice. After that, the dispersion relationship between the amplitude and the magnetotelluric impedance phase are used. This procedure is called "amplitude-phase correction" (Feldman and Ermolin 2011). Some authors implement this procedure at the stage of primary data processing (Alan Jones, 2017). The basic idea is that the same frequency ranges of the amplitude and the phase carry information about different depths (the phase is responsible for the deeper part of the cross-section). It should be noted that this procedure is correct only for the areas where there are no obvious violations of the dispersion relations in the impedance tensor.

The curve in figure 5c is of an adequate quality. We can use this curve for analysis and interpretation just after removing only the value at 1.5 kHz.

## CONCLUSIONS

We have analyzed the AMT amplitude spectra in the dead band in Chukotka summer fieldwork. Local maximum within the dead band in the daytime (2.2 and 2.6 kHz frequencies) have been described. The daytime records can be used only if the curve in the local maximum (2.2-2.6 kHz) can be reconstructed. As a rule, it is necessary to carry out measurements in the daytime for not less than 3 hours. Also, no more than 2-3 frequencies on both sides of the local maximum should be defective.

It is possible that the continuous registration of time series at high frequencies and improving the ways of magnetic sensor installation will allow decreasing measurement length in the daytime and increasing data quality in the dead band. For equipment, it is currently important to perform operative amplitude spectra visualization immediately after performing measurements on the site.

## REFERENCES

Berdichevsky MN and Dmitriev VI (2008) Models and methods of magnetotellurics. Springer-Verlag, Berlin, Heidelberg

Jones A (2017) Magnetotellurics: Status Quo and Quo Vadimus. DMEC Exploration 2017 Abstr 11: 139-158

Ermolin E, Ingerov O and Savichev A (2014) Gold exploration in Chukotka region by using audiomagnetotellurics. 22-nd EM Induction Workshop, Weimar, Germany Abstr

Feldman I and Ermolin E (2011) Amplitude-phase correction of magnetotelluric impedance curves. Journal of Mining Institute T 194: 200-210

# Improved algorithm of Frequency Domain Independent Component Analysis for Magnetotelluric data processing

S. Sato[1], T. Goto[1]
[1]Kyoto University, sato.shinya.27s@st.kyoto-u.ac.jp

**Summary**

MT data often contain noises triggered by human-activity, sensor vibration and measurement equipment. The contaminated noises have quasi-stationary characteristics (i.e., confused continuously) and cannot be removed by conventional method based on “robust stacking”. To separate these noises and MT signals, we focused on Frequency Domain Independent Component Analysis (FDICA), which can decompose independent signals from multi-component observed data, and we developed algorithm of FDICA for MT data processing (FDICA-MT). To evaluate the noise reduction performance of FDICA-MT, raw MT data obtained at Kakioka Magnetic Observatory, Japan was analyzed. Compared with MT response functions at Kakioka derived using conventional method, the ones derived using FDICA-MT are changing smoothly through frequencies and with smaller estimated errors. To test the robustness of FDICA-MT performance, we added various synthetic noises to the MT data at Kakioka and applied FDICA-MT to them. This test showed that FDICA-MT can maintain its high performance with more stability than conventional method. This advantage of FDICA-MT is suitable for MT data analysis with severe noise condition, for example, time-lapse MT surveys and MT surveys near cultural areas.

**Keywords:** Noise reduction, Independent Component Analysis

# Improvement in magnetotelluric data processing by two novel pre-stacking data selection criteria

A. Platz[1,2] and U. Weckmann[1,2]
[1] Helmholtz Centre Potsdam – German Research Centre for Geosciences (GFZ), Germany
[2] University of Potsdam, Institute of Geosciences, Germany

**SUMMARY**

Magnetotelluric (MT) measurements in populated regions suffer from severe electromagnetic (EM) noise overprinting the desired natural field variations. Typical MT data processing involves the recorded time series being divided into segments (events) for which we compute spectral values. Subsequently those spectra are averaged in a statistical manner to obtain MT transfer functions (TFs). Available approaches e.g. robust statistics, remote reference or multi station analyses try to remove outliers or uncorrelated noise. However, we have observed that intermittent noise often forms a separate distribution of TFs overlaying the true MT distribution. Ultimately, even robust statistics will fail since events within this noise cluster cannot be regarded as outliers and constitute a significantly large amount of events. In the past, these events have been removed in time and/or frequency domain prior to robust stacking. Unfortunately, this process was always tedious, non-automatic and depended on the experience and the diligence of the practitioner.

Here, we present two novel pre-stack data selection criteria for the detection of noise, outliers and EM noise clusters. The first criterion is statistically motivated and removes events with a large distance to an estimated data centre applying the covariance matrix. For this purpose, we utilise the Mahalanobis distance, whereby data centre and covariance matrix a calculated using a modified deterministic minimum covariance determinant algorithm. This criterion is able to remove scattered data points as well as reject complete data cluster originating from noise sources. The second criterion is physically driven and eliminates data points caused by a strongly polarised magnetic signal.

We will present contaminated MT stations, visualise and discuss different noise and demonstrate the application of both criteria. In many cases, they yield significant improvement in TF estimation in an automatic manner; however, we will also discuss limits of this approach and possible future developments.

**Keywords:** Magnetotellurics, data processing, EM noise removal

# Instrument Tsikl 8, flexible sensors and selected results

Zakharkin A.K.[1], Sekachev M. Yu.[2], Vechkapov O.P.[3] and Hallbauer-Zadorozhnaya, V.[4]

[1]Tsikl-geo.com, Novosibirsk, Russia, Zaharkin@ngs.ru
[2]Tsikl-geo.com, Novosibirsk, Russia smu02@mail.ru
[3]Tsikl-geo.com, Novosibirsk, Russia, oleg@eltageo.com.
[4]Tswane University of Technology, Pretoria, South Africa, valeriya.hallbauer@gmail.com

## SUMMARY

The instrument Tsikl is designed and manufacturing by Tsikl-Geo Ltd (ex Elta-geo), Novosibirsk, Russia. The company develops the geophysical technologies over 30 years. The main activity is development and manufacture of instruments and software for electromagnetic and induced polarization methods. The wide time range of effective measuring (from tens of microseconds to tens of seconds) allows use of this system for a broad spectrum of geophysical challenges. With large transmitter loops with sizes of 400-800 meters and powerful transmitters it allows to reach depths of 2-3 km so it is usable for oil and gas explorations, such as: - studying of geological structure of sedimentary basins; - detection of collectors; - structural geo-mapping. More productive shallow technology options with smaller dimensions transmitting loops 20-200 m provide a depths range 50-1000 m. So the small system is usable for: - ore bodies and kimberlite pipes explorations; - hydrogeology surveys: - engineering geology, ecology, mapping areas of salinization, etc. Unique construction of receiver loops (sensors) allows considerably decrease size of transmitter loops and applied electrical current. Using sensors of various effective areas is possible to obtain information from depth of 30-50 m to several hundred meters and more. Small size and solid frame of receiver loops allows for the measurement of all the components of electromagnetic field. Examples of application of TEM in South Africa using Tsikl 8 are presented in the abstract. One of the examples is a thin (7-10 m) kimberlite fissure located quasi horizontally in a high resistive basement. Resistivity of the fissure is slightly lower than the basement and only horizontal components can be used for delineation of this object. The second target is water saturated fracturing zone in Karoo basin. The dipping fracture has been traced from 50 m until 500 m using two sensors with effective areas 625 $m^2$ and 6400 $m^2$.

**Keywords:** TEM, electromagnetic, instrument, kimberlite fissure

## INTRODUCTION

There are many companies developing and manufacturing instruments for electrical and geoelectrical geophysical methods. Most of the instruments are very good, reliable and provide high electromagnetic interference suppression. However most of the instruments have some limitations: some of them are intended for near surface or deep survey. For many types of instruments corresponding receiving loops have not been designed, and usually a single cable is used. It greatly limits the depth of penetration of the electromagnetic field. As a consequence, to achieve the projected depth of investigation the current and/or size of transmitter loop must be increased.

## INSTRUMENT TSIKL8

The Tsikl8 is the newest instrument of this kind; it consists of several modular components, namely receiver, transmitter, module of current transmitter control and inductive sensors (receiver loops) (Figure 1).

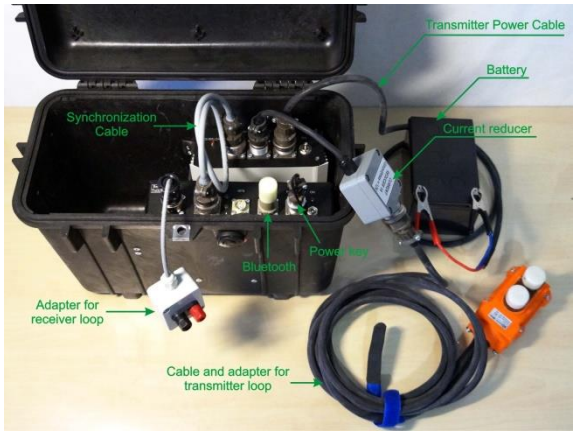


**Figure 1.** Instrument Tsikl 8 in rugged box.

**Receiver.** The receiver version with internal GPS synchronization module named as Tsikl R8 (Figure 2). The Tsikl R8 is dedicated for measuring and storing a signal received from inductive sensors. Receiver Tsikl R8 can control transmitter through a cable or if receiver and transmitter are spaced-apart for a long distance they can be synchronized by GPS synchronization systems.


**Figure 2**. Tsikl R8 receiver.

The special feature of Tsikl receivers is the technique of sequential integration of input signal. A width of integration intervals increases gradually from microsecond to few milliseconds. The significant thing is that integration time increases simultaneously with decreasing of rate of signal change and decaying of signal. The variable integration duration is adapted to the behavior of the signals and allows suppression of an electromagnetic interference very effectively with minimal distortion of the signal. Moreover the Tsikl receiver calculates and sets an optimal gain for each integration interval before AD conversion. Such technique provides us a very wide dynamic range: from a few volts to dozens of nanovolt when measuring a periodic EM signal. In most cases it is not required to post-process the recorded emf arrays so that the operator working with Tsikl Receiver may estimate a waveform of transient emf instantly after stacking and even during stacking. The specification of the receiver Tsikl R8 is presented in the Table 1.

**Table 1**. Specification of Tsikl8

| | |
|---|---|
| Dynamic range of measuring a transient EMF, min | 160 dB |
| Self- noise of the measuring channel at short-circuited input: | |
| in a 100 kHz band, max | 0.5 μV |
| in a 1 kHz band, max | 0.1 μV |
| Maximum measurable voltage value | 4 V |
| Time range of measurable transient EM process | 0.4μs – 50 s |
| Suppression of 50/60 Hz industrial interference | 80 dB |
| Voltage of external power source | 9-16 V |
| Battery life | 8 hrs |
| Power consumption | 1.5 W |
| Weigh with batteries | 2.5 kg |
| Synchronization with transmitter | Cable/ GPS |
| Connection with computer via | RS232,USB or Bluetooth |
| Overall dimensions | 145×220×55 mm |

**Transmitter.** The transmitters (Figure 3) are designed to form a rectangular pulse current in transmit loops. The typical form of current is bipolar rectangular pulses with a pause between pulses. The main properties that characterize the transmitter are the maximum power and speed of the current in the transmit loop. Each type of transmitter corresponds to a defined range of survey depths. The Tsikl-Geo ltd produces three types of transmitters of different power:

- Tsikl T20 power of 1 kW
- Tsikl T50 power of 4 kW
- Tsikl T200 power of 90 kW


**Figure 3**. Transmitter Tsikl T20 power of 1 kW

**Sensors.** A compact receiving sensor replaces big receiving loop (Figure 4).


**Figure 4**. Sensor (receiver loop) effective area 625 $m^2$, size 0.8x0.8 $m^2$

In comparison with the traditional loop, PDI sensor (loop) essentially saves a geophysicist time due to portability and the possibility of installation at several data acquisition sites. The precision geometry of the frame provides the stability of measurement results.
Of course a bandwidth of a multi turn loop is narrower in comparison with an one turn wire loop. Because of that there are a number of PDI sensor types available with different moments. They are dedicated for different initial measurement times and different depths of investigation, so it is possible to choose an optimal sensor model for any specific condition. There are several types of sensors as shown the Table 2.

**Table 2**. Specification of inductive sensors

| | PDI 400 | PDI 100 | PDI 50 | PDI 20 |
|---|---|---|---|---|
| Depth range, m | 200-3000 | 50-800 | 20-500 | 10-100 |
| Equivalent surface area | 160000 m2 | 10000 $m^2$ | 625 $m^2$ | 400 $m^2$ |
| Initial measurement time | 1 ms | 100 µs | 50 µs | 10 µs |
| Type of construction | Soft square | Rigid square | | |
| Dimension | | 0.8 x 0.8 $m^2$ | | |
| Weight | 16 kg | 5 kg | | 4 kg |

Measured signals TEM are visualized on the display of a portable PC (Figure 5).

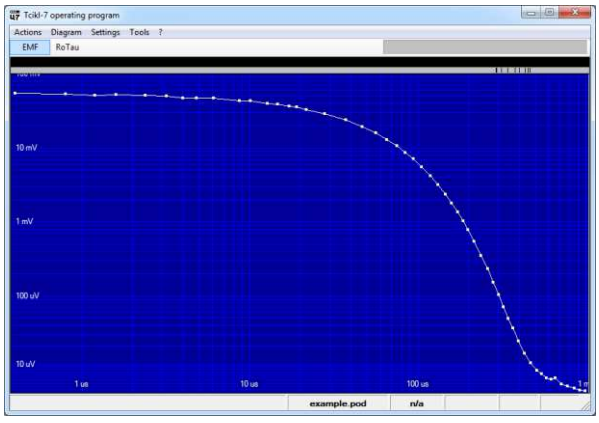

**Figure 5**. Example of visualization of field emf

**Software. Software PROBA** is meant for preprocessing of measuring results of TDEM, its quality rating, run-through and analysis of field material as transforms, and preparation of data to be interpreted in the PODBOR system. In the version Proba_10 presents curves of resistivity as a function of depth $\rho(H_{eff})$ ~~$\rho(H_{eff})$~~ for measuring configuration "loop-in-loop". These curves are the result of the fast approximate 1D inversion based on Christensen's algorithm. 1D inversion models are good starting models for other phases of the inverse solution (http://tsikl-geo.com/en/proba/).

## SELECTED APPLICATIONS OF TSIKL

We present some geological results obtained in South Africa using instrument of Tsikl series.

### 1. Delineation a kimberlite fissure in Mokopane site, Limpopo province, South Africa

The aim of the research is to delineate a kimberlite fissure. This fissure is very long and extends for more than 100 km. However, the thickness of the fissure is very narrow (about 3 – 7 m) and edge depth of the fissure is 20-30 m. Most of the fissures in South Africa are quite resistive (about 100 Ohm.m) and surrounded by host rocks (dolerites and granites) with very high resistivity (500-1000 Ohm.m and more). Laboratory measurements showed that polarization of fresh kimberlites are high. In spite of success with results obtained using TEM FAST 48 with coaxial loop (Hallbauer-Zadrozhnaya, 2016) we made a small experiment with Tsikl8. The kimberlite fissures in South Africa are mostly vertical. It means for its delineation the component dBz/dt is not effective. It comes from the theory of electromagnetic wave propagation and results from field work. Obviously the best component is one of the horizontal components. It is known that the components do not exist in the horizontal uniform media whereas this component of EM field is always present in inhomogeneous media. We accept that the fissure is oriented in the x direction, which is known from the geology of this area and then the dBy/dt component can be used. We used a large transmitter loop (50 x 50 m) and portable mobile sensor with effective area 80 x 80 m. We recorded 3 components of electromagnetic field: dBz/dt, dBy/dt and dBz/dt. Receiver was moved along the profile inside of the transmitter loop with steps equal to 1 m.

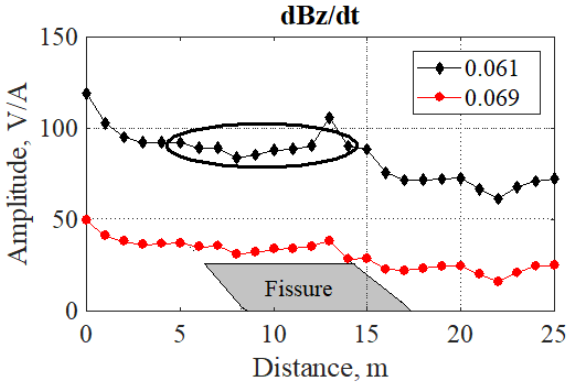


**Figure 6**. dBz/dt signals at the time 0.061 ms and 0.069 ms. Part of the profile 7

Comparison of obtained data shows that the dBy/dt amplitude is much larger than traditionally measured dBz/dt (Figures 6 and 7). Drilling was carried out within the identified anomalies and the fissure was opened at a depth of about 25 m.

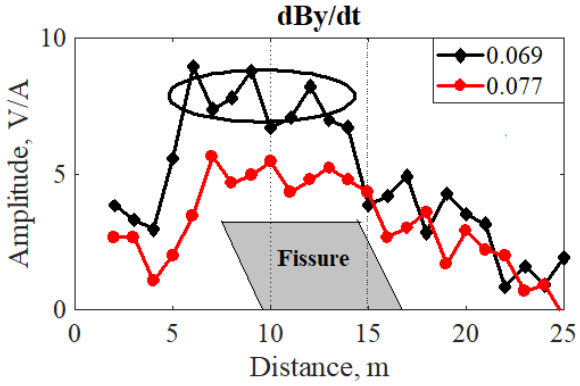


**Figure 7**. dBy/dt signals at the time 0.069 ms and 0.077 ms. Part of the profile 7

**2. Detection of aquifers above and below dolerite sills, Eastern Cape, South Africa.**

TEM sounding were carried out in the Qoqodala area of Western Cape with the aim to detect deep-seated structures which could contain water bearing sediments, as well as identification of the borders between dolerite sills and surrounding sediments [Hallbauer-Zadorozhnaya et al., 2004]. Field measurements were carried along the profile for 1100 m, with part of the profile located on the mountain, and another part located in the valley. The instrument Tsikl 5 had been used. The size of the transmitter loop was 100 x100 m and receiver loop 625 m in the mountain area (left part of profile, TEM 5-21) (Figure 8).

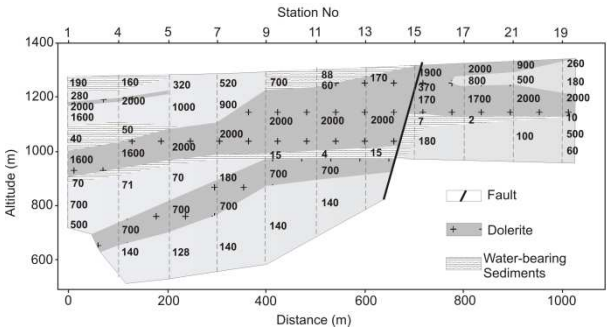


**Figure 8.** Geoelectrical section along the profile. Qoqodala site, instrument Tsikl, transmitter loops 10 x 10 m and 200 x 200m.

In the valley where the thickness of low conductive sediment increases (TEM 1-4) the transmitter loop of 200 x 200 m and receiver loops 625 and 6400 m2 allows investigation up to 600 m. There are a few boreholes, and drilling still continues. Water bearing sediments are present both, above and below a dolerite sill. Most of the TEM signals were distorted by induced polarization effect. For interpretation of TEM data the software ERA (Epov and Eltsov) and homemade calculating program IRAF (Hallbauer-Zadorozhnaya) were used. An existing fault can clearly be seen on the TEM curves: shapes of curves are different on both sides of the fault. Several lenses and layers with a reduced resistivity have been identified, on some of them the presence of water was confirmed by drilling, some are perspective at depth more than 600 m.

## CONCLUSIONS

The instrument Tsikl is designed and manufactured by Tsikl-Geo Ltd (ex Elta-geo), Novosibirsk, Russia. The company developed the geophysical technologies over 30 years. The wide time range of effective measuring (from tens of microseconds to tens of seconds) allows use of this system for a broad spectrum of geophysical challenges. The special feature of Tsikl receivers is the technique of sequential integration of input signal. The Tsikl receiver calculates and sets an optimal gain for each integration interval before AD conversion. Such technique provides a very wide dynamic range: from a few volts to dozens of nanovolt when measuring a periodic. It is important that a compact receiving sensor with size 0.8 x 0.8 $m^2$ replaces big receiving loops 225 $m^2$, 625 $m^2$ and 10000 $m^2$. With large transmitter loops with sizes of 400-800 meters and powerful transmitters it allows to reach depths of 2-3 km. Shallow technology options with smaller dimensions transmitting loops of 20-200 m provide a depths range 30-1000 m. Selected examples of application of TEM in South Africa using Tsikl showed a workability of this instrument for delineation. One of the examples is a thin (7-10 m) kimberlite fissure located quasi horizontally in high resistive basement using horizontal positioned receiver loop. The second target is a water saturated fracture zone in the Karoo basin. The dipping fracture has been traced from 50 m until 500 m using two sensors with effective areas 625 $m^2$ and 6400 $m^2$.

## REFERENCE

Hallbauer-Zadorozhnaya V. (2016) New technology for delineation of resistive and polarizable kimberlite fissures using TEM method in South Africa. The 13rd China International Geo-Electromagnetic Workshop CIGEW2017, 9-11 November 2017, Wuhan, Hubei, China

Hallbauer-Zadorozhnaya V., Chevallier L, Nhleko L, Wheeler W., (2004). Detection of aquifers above and below dolerite sills: a successful application of TDEM in the Easter Cape. Geoscience Africa 2004. Abstr. 243-244.

# Intrinsic response of a TEM measuring unit as cause of slowly decaying anomalous transients

M. Sharlov[1] and N. Kozhevnikov[2]
[1] SIGMA-GEO Ltd., Institute of the Earth's Crust of the Siberian Branch of the RAS, sharlov@sigma-geo.ru
[2] Institute of Petroleum Geology and Geophysics of the Siberian Branch of the RAS, kozhevnikovno@ipgg.sbras.ru

## SUMMARY

We illustrate and discuss decrease in the decay rate of the TEM voltage response in cases when TEM soundings are performed using central loop arrays with small-size transmitter loops. Other things being equal, this effect is the more noticeable the smaller the transmitter loop and/or the more resistive the ground. The effect is not observed when the receiver loop is located outside the transmitter loop. We show that the cause of the slowly decaying central loop TEM voltage response is the intrinsic transient response of the measuring amplifier. Inversion of the late time TEM response without regards to the intrinsic response of measuring unit results in appearance of nonexistent conductive ground layers and thus in misinterpretation of the TEM data. To reduce the intrinsic transient response of the measuring amplifier, the following may be useful: reduction of the latest measurement time, subtracting the intrinsic transient response from the total one, disconnection of the amplifier from the receiver loop during the current turnoff in the transmitter loop.

**Keywords:** TEM, transients, intrinsic response, operational amplifiers, decay rate

## INTRODUCTION

The TEM sounding method has found wide application in the hydrogeology, geotechnical engineering, permafrost and other near-surface related studies. The sounding depth may start from a few meters and reach 500 meters and more. In recent years, numerous surveys were performed in Russia over the total area of hundred square kilometres (Sharlov et al., 2017).

A TEM measuring system includes transmitter and receiver units, transmitter (TX) and receiver (RX) loops, cables, satellite or wire synchronization system, power generator, laptop, cars and other elements. During the excitation and recording of transients, the earth response is convolved with the intrinsic response of TEM system. Therefore, measuring intrinsic response of a TEM system is necessary to assess the reliability of TEM data.

Several methods are known for testing TEM systems in laboratory and field conditions (Foged et al., 2013; Sapial et al., 2015; Kozhevnikov 2012; Zakharkin, Tarlo, 1999). It is usually supposed that the contribution of the system's intrinsic response to the measured TEM response is significant only at early times and that measurements at late times are unaffected. However, we noticed some late-time response features that cannot be explained without taking into consideration an intrinsic response of the TEM measuring system (Sharlov et al., 2017; Sharlov et al., 2018).

## THEORY AND INSTRUMENTATION

As it is known, a TEM response depends on the offset **r** (1/2 length of the transmitter loop side for a central loop array or the distance between centers of the transmitter and receiver loops for a loop-loop array). At early times, central loop and loop-loop responses differ. The difference increases with larger offset **r** and lower ground resistivity. As the time progresses, diameter **d** of the region occupied by the eddy currents increases, and the distinction between central loop and loop-loop responses decreases. At late times (**d >> r**), the TEM response does not depend on the offset. However, we noticed that late time central loop and loop-loop responses coincide when using a large transmitter loop. Sometimes, when using transmitter loops with side length of 100m and less, a different situation may appear: the decay rate of transient voltage measured with central loop steadily decreases with time. The slowing of the decay rate is particularly noticeable in studies of resistive ground. This effect is manifested when using different TEM instruments (Sharlov et al., 2018). Below we give some illustrative examples of the TEM response slowing.

In our studies, we used FASTSNAP digital telemetric TEM system (Sharlov et al., 2017). This system provides measurement sampling rates up to 40 MHz. Transients are recorded and saved in the full wave-form of the decay that makes this system a suitable choice for test surveys. For processing and inversion of the TEM data we

employed TEM-Processing and Model3 software respectively (Sharlov et al., 2017).

## RESULTS

When using central loop arrays, we often observed, at late times, an unexpected decrease of EMF decay rate (Sharlov et al., 2018). Similar effect has been noted by other researchers, for example in (Geidetzka, 2002).

In order to study the late-time transient induction responses, we conducted a test TEM survey on Lake Baikal in 2017 - 2018 (Sharlov et al., 2017; Sharlov et al., 2018). Due to the fresh water depth of more than 1600 m, Lake Baikal provides a near-to-ideal geoelectric model with *precisely known* parameters (Figure 1, A). We performed the work in early spring from the ice cover at a point with a water depth of more than 1000 m. Examples of acquired TEM responses exhibiting a decrease in the EMF decay rate are shown in Figure 1 (B, C).

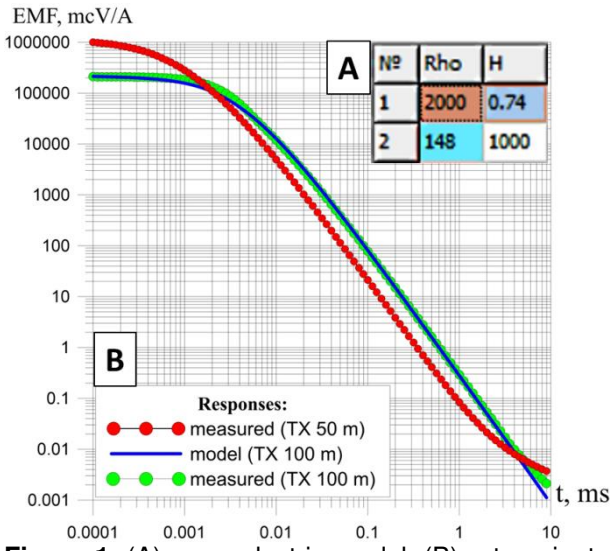


**Figure 1.** (A) – geoelectric model; (B) – transients EMF responses.

As can be seen in Figure 1B, at late times the transient voltage measured using 50m by 50m and 100m by 100m transmitter loops decays more slowly than the calculated voltage decay for the known model. The 50m by 50m decay is the slowest indicating the effect may increase progressively with decreasing transmitter loop sizes. On the apparent resistance curves (Figure 2), this effect manifests itself as a steady decrease in $\rho_a$ over time. For the arrays with transmitter loops of 100m by 100m and 50m by 50m, the anomalous decrease in $\rho_a$ becomes noticeable at $t \geqslant 4$ - 5 ms and $t \geqslant 1$ ms, respectively. Obviously, the inversion of these curves will result in a model with conductive layers which in fact do not exist.

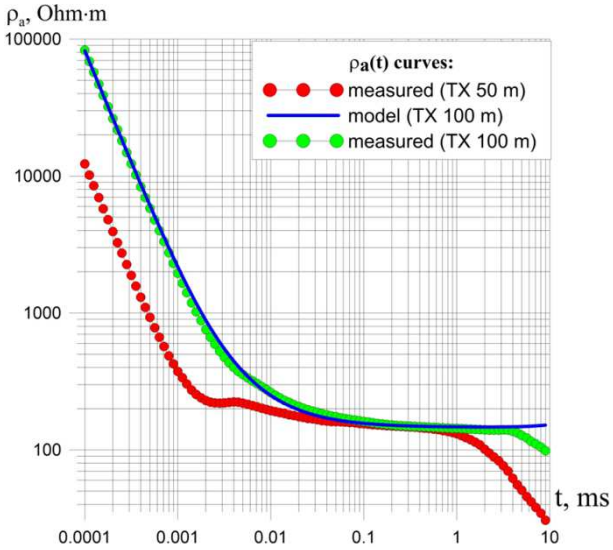


**Figure 2.** Apparent resistivity ($\rho_a$) curves.

Since the geoelectric model is known to contain no conductive layers, we concluded that the observed effect is not related to geology, but is the manifestation of intrinsic TEM system response. This effect appears at late times, when the current in the TX loop has been switched off, so we focused on studying the input circuit of the FastSnap receiver unit. The circuit includes an analog-to-digital converter AD9244 from "Analog Device" and high-speed instrument amplifier AD8138 recommended by the manufacturer.

When measuring late-time TEM response with the FastSnap equipment, large currents (up to 30 A) and gain factors are used (Sharlov et al., 2017). Thus, in measuring a late-time portion of the TEM responses shown in Figures 1 and 2, the gain was equal to 140. As it is known, supplying a voltage step to the input of an operational amplifier will cause the amplifier to output a slowly decaying transient response, or long tail (Dostal, 1981).

In order to study the transient response of measuring circuit of FastSnap receiver, we performed laboratory measurements. We supplied to the receiver input a rectangular voltage pulse with amplitude of 1 V and duration of 32 μs (pulse falling edge duration was 100 ns). Intrinsic response of measuring circuit was recorded at gain equal to 140. The shape of input voltage and measured response are shown in Figure 3.

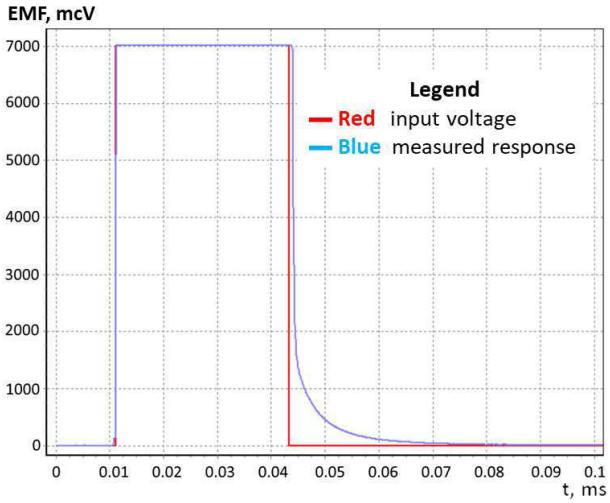


**Figure 3.** Input rectangular voltage pulse and intrinsic response of measuring circuit at gain of 140.

Figure 4 illustrates the measuring circuit's intrinsic response. At **t** = 300 μs, the slowly decaying voltage is 0.45 μV. At **t** = 7 ms it drops to 0.05 μV, which is only $5 \cdot 10^{-6}$ % of the input voltage. Figure 4 shows also a graph of power function approximating the measured response.

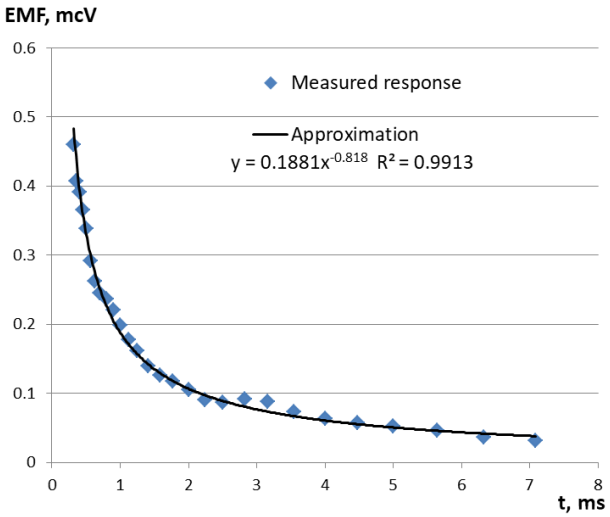


**Figure 4.** Late-time system response and its approximation by a power function.

In order to estimate the contribution of the measuring unit's intrinsic response to the total TEM response, we compared modeled and measured TEM data (Figures 5 and 6). As Figure 5 shows, the total voltage response (red plot) represents the sum of the model (green plot) and intrinsic (blue plot) responses. At late times, an anomalous slowing of the total EMF decay is clearly seen. The modeled data agree with those measured on ice of Lake Baikal, as one can see in Figure 6 which shows modeled (with allowance made for the contribution of a "long tail") and measured apparent resistivity curves.

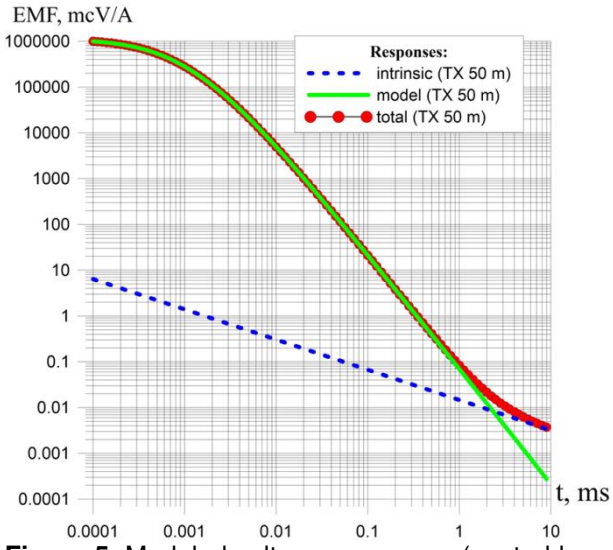


**Figure 5.** Modeled voltage responses (central loop array; 50m by 50m TX loop).

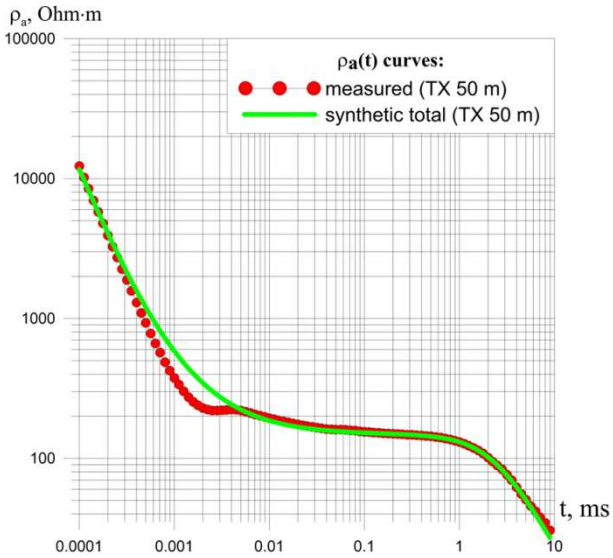


**Figure 6.** Modeled and measured apparent resistivity curves (central loop array; 50m by 50m TX loop).

In the time range 0.1 – 10 ms, mean square divergence between the measured and modeled curves does not exceed 2%.

## CONCLUSIONS

The slowly decaying intrinsic transient voltage response of the FastSnap receiver's measuring circuit leads to decrease in the decay rate of the late time total TEM response. The effect of the intrinsic response to a total one is more pronounced when using central loop arrays with small transmitter loop and/or studying resistive ground. Inversion of the late time TEM response without regards to the intrinsic response of the measuring unit results in appearance of nonexistent conductive ground layers and thus in

misinterpretation of the TEM data. In order to reduce the effect of the intrinsic voltage response on the TEM data, we recommend the following: reduction of the latest measurement time; subtracting the intrinsic transient response from the total one; disconnection of the amplifier from the receiver loop during the current turnoff in the transmitter loop.

## REFERENCES


Dostal, J. (1981) Operational amplifiers. ELSEVIER SCIENTIFIC PUBLISHING COMPANY, Amsterdam – Oxford – New York.

Foged, N., Auken, E., Christiansen, A.V., and Sørensen, K. I. (2013) Test-site calibration and validation of airborne and ground-based TEM systems. Geophysics, VOL. 78, NO. 2, P. E95–E106.

Geidetzka, A. (2002) Erste Erfahrungen mit der Nano TEM - Apparatur. Diplomarbeit, Institut für Geophysik und Meteorologie, Köln.

Kozhevnikov, N.O. (2012) Testing TEM systems using a large horizontal loop conductor. Russian Geology and Geophysics, 53, 1243–1251.

M.V. Sharlov, N.O. Kozhevnikov, R.V. Sharlov (2017) Lake Baikal – A Unique Site for Testing and Calibration of Near-surface TEM Systems. Near Surface Geoscience 3-7 September 2017, Malmö, Sweden. 5 pp. doi: 10.3997/2214-4609.201702038

M.V. Sharlov, N.O. Kozhevnikov, I.A. Shelokhov (2018). Unexpected dependence of the late-time transient response on the size and configuration of a TEM array. Engineering and Mining Geophysics – 2018. Extended Abstracts.

Sapial V., Viezzoli A., Menghini A., Marchetti M., Chiappini M. (2015) The Italian reference site for TEM methods. Annals of Geophysics, 58, 5, G0548; doi:10.4401/ag-6805

Sharlov, M.V., Buddo, I.V., Misyurkeeva, N.V., Shelokhov, I.A., Agafonov, Yu.A. (2017) Experience of efficient near-surface studies by the shallow TEM method using the Fastsnap system. Pribory i Sistemy Razvedochnoi Geofiziki 38 (2), 8 – 23.

Sharlov, M.V., Buddo, I.V., Misyurkeeva, N.V., Shelokhov, I.A., Agafonov, Yu.A. (2017). Transient Electromagnetic Surveys for High-Resolution Near-Surface Exploration: Basics and Case Studies. FirstBreak, Vol. 35, September 2017, 63 – 71.

Zakharkin, A.K., Tarlo, N.N. (1999) Metrological support of TEM measurements. Geofizka, N6, 34 – 39.

# Mapping Induced Electromagnetic Fields across the Continental United States

Benjamin S. Murphy[1] and Gary D. Egbert
College of Earth, Ocean, and Atmospheric Sciences; Oregon State University; Corvallis, Oregon, USA
[1]murphybe@oregonstate.edu

**SUMMARY**

The recent availability of high quality, three-dimensional magnetotelluric (MT) datasets has opened up many new possibilities for array processing techniques. By analyzing the large EarthScope MT dataset in conjunction with geomagnetic data from observatories and ground-based space physics experiments, we are able to map out patterns in induced electromagnetic (EM) fields on a continental scale as well as to gain new insights into the spatial and temporal patterns of source EM fields across North America. To perform this analysis, we first decompose multi-year geomagnetic time series measured across North America into spatial and temporal data modes using the frequency-domain robust principal components analysis (PCA) technique of Smirnov and Egbert (GJI, 2012). Using the robustly estimated temporal modes, we then solve a linear parameter estimation problem to find the linear combinations of individual MT site frequency-domain components that best reproduce the PCA-derived temporal modes during the time period in which that individual MT site was operating (generally just a few weeks). The coefficients of these linear combinations represent the components of the spatial data mode at the given MT site. These spatial modes can then be sorted into the two traditional “plane-wave” modes (horizontal magnetic fields polarized N-S and polarized E-W) and higher-order gradient modes. As of this writing, more than 1000 EarthScope MT sites covering almost two-thirds of the contiguous United States are available for this analysis. The “plane-wave” spatial data modes, when derived for this entire dataset, provide a continent-scale view of induced EM fields. As continent-scale MT data inversion is still impractical, the derived maps of induced fields contain valuable information about continental-scale geoelectric structures. The higher-order spatial data modes as well as the temporal data modes provide new insights into characteristics of the natural source fields.

**Keywords:** array processing, anomalous fields, EarthScope

# Measurement of the magnetic field with moving carriers

F. Dudkin, V. Pronenko and V. Korepanov
LLC LEMI, Lviv, Ukraine, vakor@isr.lviv.ua

**SUMMARY**

The geophysical research of Earth's crust structure or local anomalies detection requires measurements of the Earth's magnetic field vector variations. To decrease time and money expenses, recently the attempts to do this with the help of moving carriers with the use of FGM onboard are known. Such a method faces a number of difficulties that limit the FGM application and measurement precision. The conditions of FGM use and peculiarities of their operation onboard moving carriers and errors sources are studied. The method of reduction of rotating measuring axes to a basic orientation is presented; an example of necessary sensitivity calculation at small anomaly detection is given. The requirements to customized FGM for light moving carriers are discussed.

**Keywords:** magnetic field, moving carrier, flux-gate magnetometer

## INTRODUCTION

The aeromagnetic prospecting is a widespread method used for productive survey of large territories or areas with the difficult access (forests, swamps, shallow waters). It is based on the difference in the magnetic properties of soils and rocks, which were magnetized by geomagnetic fields at present or ancient time (Broughton Edge and Laby 2012). The magnetization level is usually determined by the presence of ferromagnetic minerals. Now, a new type of mobile carriers – small remotely piloted vehicles or drones – is becoming very common. Additionally, the drones equipped with magnetometer turn out to be very efficient for: the soil magnetic properties mapping (Dobos et al. 2006); a location of the archeological sites investigation (Linford 2009); the detection of buried metallic objects (UXO, EOD, landmines etc.) (Pasion et al. 2009); the wetlands aeromagnetic inspection (Dyson et al. 2007); the underground utility location (steel and concrete constructions (Fassbinder 2011), buried DC and AC power cables etc. (Sun et al. 2014).

The magnetic fields of the most of these objects are very low (a few nT or less) and so first need at their measurements is a very sensitive magnetometers which should have small mass and dimensions. Very often, at data processing and interpretation, it is necessary not only an object detection but also its classification, what needs the use of inverse problem technique. Obviously, such a technique is the most effective at the maximum given values; i. e. 3D field configuration and space position both the magnetic sensors and air-ground boundary. Let us discuss the peculiarities of magnetometers operation onboard moving carriers.

## THE MAGNETOMETER TYPE SELECTION FOR DRONE

The most sensitive for drone version are the scalar magnetometers (for example, Cesium-vapor magnetometer G-822A has noise less than 0.001 nT/√Hz rms at a 0.1 second sample rate (Geometrics, OYO Corporation)). Unfortunately, such magnetometers significantly limit the possibility of inverse problem solution at data interpretation, for lack of information about the magnetic field Cartesian components. Additionally, a potential sensitivity threshold of the Cesium magnetometers is practically unrealized due to high level of magnetic field interference from a carrier motor operation and movement.

We believe that 3-component fluxgate magnetometers (FGM) seem to be the most preferable for drone applications by reason of less weight, power consumption and costs at insignificant loss in sensitivity relatively to the scalar ones. However, the serious problem at FGM field application is the interference due to FGM orientation instability: during movement of FGM, mounted on a boom fixed to a drone, the permanent attitude changes in the Earth's magnetic field leads to corresponding changes of its projection on FGM axes. For example, the angular deviation of FGM sensor about 0.01° can give a parasitic signal up to 5-12 pT. At the same time, a minimal anomalous magnetic field at geomagnetic soil mapping can achieve a value

$$B_{min}=\kappa B_0 \approx 10^{-5} B_0 = 0.3\text{-}0.7 \text{ pT}, \quad (1)$$

where κ is the soil magnetic susceptibility (Scott, 1983), $B_0$ is the absolute value of the Earth's

magnetic field vector), that is about of order less than parasitic signal for such a tiny angular deviation. Also the electromagnetic interference from a drone motor, uncontrolled FGM oscillations relatively ground surface are the limiting factors of the magnetometer sensitivity level. Indicated interference significantly exceeds the threshold level which is necessary for detection and classification of studied objects and so should be previously estimated and then decreased by proper methods.

## VECTORIAL MAGNETOMETERS USE PECULIARITIES ONBOARD MOVING CARRIER

So, practice requires the problem solution for application of vectorial magnetometers with moving carriers both for provision of the magnetometer's high sensitivity level and for reduction of 3-component data from arbitrary moving Cartesian coordinate system to fixed coordinate system linked with the Earth. That is why the realization of FGM operation on drones for specified applications presents a complicated technical problem.

Two approaches for FGM application are considered below. The first one relates to geomagnetic prospecting, where the large areas with slow change of the soil magnetic susceptibility are studied. In this case the measurement of anomalous magnetic field components is not so important because of absence of the pronounced structural configurations. Such a study can be provided in magnetic field absolute value measurement mode, for example, by single FGM suspended under a small autonomous copter. The anomalous magnetic field value $\Delta B_i$ is calculated by simple equation

$$\Delta B_i = B_i - B_1, \quad (2)$$

where $B_1$, $B_i$ are the first and $i^{th}$ magnetic field absolute value readings on the studied profile, $B_i = (B_{x,i}^2 + B_{y,i}^2 + B_{z,i}^2)^{0.5}$. Here the influence of permanent change of FGM orientation on $\Delta B_i$ calculation has to be studied.

The second approach is applied at fast magnetic susceptibility changes, for example for detection of subsurface local objects, landmines or UXO/EOD (Korepanov and Dudkin, 2016). In this case the 3-component magnetic field measurements are preferable for increase of classification probability for detected objects. So the reduction of magnetic field component measured by moving and rotating FGM to some standard directions is required. This procedure can be provided with use of the second ground-based (fixed) magnetometer. The idea of this method can be explained by the following equations. Each matrix $\mathbf{A}=[a_{mn}]$, which describes the rotating system can be presented in the form

$$\mathbf{A} = \begin{bmatrix} \cos\alpha\cos\gamma - \sin\alpha\cos\beta\sin\gamma & -\cos\alpha\sin\gamma - \sin\alpha\cos\beta\cos\gamma & \sin\alpha\sin\beta \\ \sin\alpha\cos\gamma + \cos\alpha\cos\beta\sin\gamma & -\sin\alpha\sin\gamma + \cos\alpha\cos\beta\cos\gamma & -\cos\alpha\sin\beta \\ \sin\beta\sin\gamma & \sin\beta\cos\gamma & \cos\beta \end{bmatrix}, \quad (3)$$

where $\alpha$, $\beta$, $\gamma$ are precession, nutation and proper rotation angles (Euler's angles). If the direction of the Earth magnetic field is known (for example from a reference ground magnetometer) then the direction of rotation axis can be calculated. Let the rotation ort is $\mathbf{n}=(n_x, n_y, n_z)$, where x, y, z relate to the fixed coordinate system and $n_x$, $n_y$, $n_z$ are the ort directional cosines. Then the rotation matrix can be written in the form

$$\mathbf{A}(\mathbf{n},\varphi) = \begin{bmatrix} \cos\varphi + (1-\cos\varphi)n_x^2 & (1-\cos\varphi)n_x n_y - (\sin\varphi)n_z & (1-\cos\varphi)n_x n_z + (\sin\varphi)n_y \\ (1-\cos\varphi)n_x n_y + (\sin\varphi)n_z & \cos\varphi + (1-\cos\varphi)n_y^2 & (1-\cos\varphi)n_y n_z - (\sin\varphi)n_x \\ (1-\cos\varphi)n_x n_z - (\sin\varphi)n_y & (1-\cos\varphi)n_y n_z + (\sin\varphi)n_x & \cos\varphi + (1-\cos\varphi)n_z^2 \end{bmatrix}, \quad (4)$$

where φ is the rotation angle of a magnetometer around ort **n**.

Also the quaternion representation for description of rotating magnetometer data can be used. It allows avoiding the uncertainty of the Euler angles application by description of rotating magnetometer data in 4D space with use of hypercomplex numbers (Morais et al. 2014). If $\mathbf{\Lambda}=(\lambda_0, \lambda_1, \lambda_2, \lambda_3)$ is quaternion, where $\lambda_m$, m=0, 1, 2, 3 are quaternion components then rotation matrix can be presented in the form:

$$\mathbf{Q} = \begin{bmatrix} 1-2\lambda_2^2-2\lambda_3^2 & 2\lambda_1\lambda_2 - 2\lambda_3\lambda_0 & 2\lambda_1\lambda_3 + 2\lambda_2\lambda_0 \\ 2\lambda_1\lambda_2 + 2\lambda_3\lambda_0 & 1-2\lambda_1^2-2\lambda_3^2 & 2\lambda_2\lambda_3 - 2\lambda_1\lambda_0 \\ 2\lambda_1\lambda_3 - 2\lambda_2\lambda_0 & 2\lambda_2\lambda_3 + 2\lambda_1\lambda_0 & 1-2\lambda_1^2-2\lambda_2^2 \end{bmatrix}. \quad (5)$$

If **A** is a rotation matrix around ort **n** for transformations of Equations 4-5 then vector components measured by a rotating magnetometer can be calculated by equation

$$B_m = \mathbf{A}^T B_n, \quad (6)$$

where $\mathbf{A}^T$ is transposed matrix, $B_m$ and $B_n$ are the magnetic field components reduced to base coordinate frame and measured by the rotated magnetometer respectively.

However the transformations of Equations 3-5 do not give possibility for calculation of the anomalous magnetic field components, which can be associated with magnetic susceptibility changes induced, for example, by buried compact object or UXO (only the deviation of the absolute value for anomalous magnetic field vector may be found). It is connected with the rotation operation of a total magnetic field vector, which is the sum of the Earth and anomalous magnetic fields, relatively the Earth magnetic field vector of the base magnetometer. Additional information about magnetic field components it is possible to get from dual axis inclinometer, for example SCA100T (http://www.mouser.com). The maximum error of rotation angle calculation (Δθ, in degrees) can be estimated from simple relation

$$\Delta\theta \le (180/\pi)|\Delta\mathbf{B}|/|\mathbf{B_0}|, \quad (7)$$

where $\Delta\mathbf{B}$ and $\mathbf{B_0}$ are vectors of the anomalous and the Earth's magnetic fields. For example, at $|\Delta\mathbf{B}|$=10 nT and $|\mathbf{B_0}|$=50,000 nT the angular error is less than 0.01°.

The better opportunity to measure the anomalous field values seems to present the use of a differential system of two FGMs. Let us examine the case of detection of a steel sphere of radius R=1 cm with magnetic permeability $\mu_s=300\mu_0$, where $\mu_0=4\pi\times10^{-7}$ H/m is the absolute magnetic permeability of free space. After both FGMs axes reduction the components of the anomalous magnetic field can be calculated by following Equations:

$$\Delta\mathbf{B}=\mathbf{B}_2-\mathbf{B}_1, \quad (8)$$

where $\mathbf{B}_2$ and $\mathbf{B}_1$ are the reduced magnetic field vectors measured by front and rear FGMs respectively. They are calculated by Equations:

$$B_{k,m}=a_k\mathbf{D}M_m, \quad (9)$$

index k=1, 2 relates to front and rear FGMs respectively, m=x, y, z; $a_k=\mu_0/(4\pi r_k^5)$, $r_k=((x-\Delta x\delta_{2k})^2+y^2+z^2)^{0.5}$, Δx is the boom length, $\delta_{2k}$ is the Kronecker symbol, $\mathbf{D}=[d_{ij}]$ is coordinate matrix, $d_{11}=2(x-\Delta x\delta_{2k})^2-y^2-z^2$, $d_{12}=d_{21}=3(x-\Delta x\delta_{2k})y$, $d_{13}=d_{31}=3(x-\Delta x\delta_{2k})z$, $d_{22}=2y^2-(x-\Delta x\delta_{2k})^2-z^2$, $d_{23}=d_{32}=3yz$, $d_{33}=2z^2-(x-\Delta x\delta_{2k})^2-y^2$, $M_m$ is a matrix of Cartesian components of the steel sphere magnetic moment (Fitzpatrick 2016),

$$M_m=4\pi R^3(\mu_s-\mu_0)B_{0,m}/(\mu_0(\mu_s+2\mu_0)), \quad (10)$$

$B_{0,m}$ is a matrix of Cartesian components of the Earth's magnetic field.

## TEST RESULTS AND FGM SELECTION

The results of anomalous magnetic fields calculation for movement of two FGMs placed on a boom with separation distance Δx=1 m over the steel sphere R=1 cm with centre coordinates $x_s=y_s=z_s=0$ at height z=0.5 m along x-direction (y=0) are shown in Figure 1. Here for simplification of numerical estimations we assume $B_{0,m}$=50,000 nT. From these Figures it is clearly seen that such a small object can be reliably detected if the FGM noise level is less than 0.15 nT. It should be noted that calculated anomalous fields is proportional to $R^3$, thus for steel sphere of R=2 cm the field maximums are in the range 3-6.4 nT. The same field intensity can be achieved at R=1 cm and z=0.25 m because of field proportionality to $1/r^3$.

Additionally to low noise level, the broadening of FGM frequency range up to 60 Hz is necessary because of drone movement and for to create the opportunity of AC cables detection. Next requirement is the minimization of the FGM power consumption with retention of low noise level and wide frequency range.

For satisfaction to all enumerated requirements for drone-mounted FGM the LEMI-026 magnetometer was developed. Its main parameters are: noise level 10 pT/Hz$^{0.5}$ at 1 Hz; sampling rate is 250 Hz; 32 bit ADC (6 channels); maximal power consumption is 1.2 W; recording time with 1900 mAh internal battery about 5 hrs; weight is less than 1.25 kg; dimensions of electronic unit with sensor and battery are Ø 96×270 mm. The field tests of the LEMI-026 FGM were performed (Prystaj et al. 2016). For calculation of LEMI-026 orientation in space the second FGM placed on the ground surface and the SCA100T dual axis inclinometer with 0.0025° resolution were used. The experimental tests were performed which confirmed the LEMI-026 FGM applicability for magnetic survey with small drones.

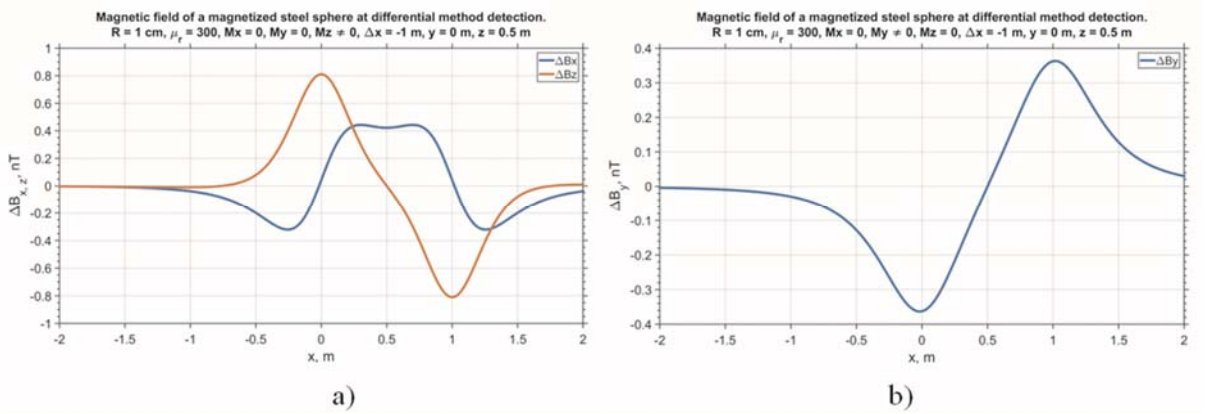


**Figure 1.** Magnetic field of a magnetized steel sphere at differential detection method: a) $B_x$ and $B_z$-components; b) $B_y$-component.

## Conclusions

The theoretical study and calculations results given above confirm that it is possible to estimate with necessary resolution the anomalous magnetic field measured in movement by a vector magnetometer mounted onboard of a small carrier such as drone. The method of the reduction of rotating components to basic ones is described and estimation of obtainable sensitivity is given. Basic requirements to a drone-portable FGM are outlined.

## References

Broughton Edge AB, Laby TH (2012) The Principles and Practice of Geophysical Prospecting. Cambridge University Press.

Dobos E, Carré F, Hengl T, Reuter HI, Tóth G (2006) Digital Soil Mapping as a support to production of functional maps. EUR 22123 EN, Office for Official Publications of the European Communities, Luxemburg.

Dyson L, Johnson C, Heppell E, Pieters M (2007) Archaeological evaluation of wetlands in the Planarch area of North West Europe. http://agris.fao.org/agris-search/search.do?recordID=AV20120155498.

Fassbinder JWE (2011) Geophysical Prospection: a Powerful Non-destructive Research Method for the Detection, Mapping and Preservation of Monuments and Sites, in Proceedings of the 1 st CEUR Workshop on The New Technologies for Aquileia, Aquileia, Italy, May 2, 2011, 1-9.

**Fitzpatrick R (**2016) **Classical Electromagnetism.** ISBN 978-1530325917, CreateSpace Independent Publishing Platform, 228.

Geometrics, OYO Corporation http://www.geometrics.com/geometrics-products/geometrics-magnetometers/.

http://www.mouser.com/pdfdocs/sca100t_inclinometer_datasheet_8261800b2_0.pdf.

Korepanov V, Dudkin F (2016) Magnetometer design for copters. Proceedings of the 2nd International Conference on Sensors Engineering and Electronics Instrumental Advances (SEIA' 2016), 22-23 September 2016, Barcelona, Spain: 138-139.

Linford N (2009) Archaeogeophysics: Applications and challenges for magnetic methods. Proceedings of the Workshop on Soil Magnetism: Multidisciplinary Perspectives, Emerging Applications and New Frontiers: Report. ERDC Report: 35-36.

Morais JP, Georgiev S, Sprößig W (2014) Real Quaternionic Calculus Handbook, ISBN 978-3-0348-0622-0, Birkhäuser Basel, 216.

Pasion LR, Billings SD., Oldenburg DW, Li Y, Lhomme N (2009) Soil compensation techniques for the detection of buried metallic objects using electromagnetic sensors. Proceedings of the Workshop on Soil Magnetism: Multidisciplinary Perspectives, Emerging Applications and New Frontiers: Report. ERDC Report, 64.

Prystai A, Korepanov V, Dudkin F, Ladanivskyy B (2016) Vector Magnetometer Application with Moving Carriers. Sensors & Transducers, Vol. 207, Issue 12: 44-49.

Scott JH (1983) Electrical and magnetic properties of rock and soil. Report 83-915, Prepared in cooperation with the U.S. Air Force, 44.

Sun X, Hou Y, Pong PWT (2014) Underground Power Cable Detection and Inspection Technology Based on Magnetic Field Sensing at Ground Surface Level. IEEE Transactions on Magnetics, Vol. 50, Issue 7, **doi:**10.1109/TMAG.2013.2297195.

# The variation of the peak frequency of Schumann Resonance(SR) observed at five stations in the Control Source Extremely Low Frequency (CSELF) network

Han Bing[1], Tang Ji[1], Zhao Guoze[1], Wang Lifeng[1], Chen Xiaobin[1]
[1]
State Key Laboratory of Earthquake Dynamics,
Institute of Geology, China Earthquake Administration, Beijing, China, zddhb@163.com

**SUMMARY**

With the support the Wireless Electro-Magnetic Method (WEM) project, we built the first Control Source Extremely Low Frequency (CSELF) continuous observation network which include 30 electromagnetic stations in Beijing Capital Area and Southern Section of North-South Seismic Belt in China for the artificial and nature source singles recording. This study focus on the natural source electromagnetic spectrum in frequency band ranged from 3 to 48Hz, and the Schumann resonance and six harmonic frequencies can be observed clearly. We analyzed the peak frequency change during last two and a half years in five stations. Fourier transform method was applied to the whole day's original 256Hz time series to get the electromagnetic spectrum and after that we identified the local maximum value and its corresponding frequency value for SR fundamental and the harmonic mode everyday and we can observe the frequency value change over time. For getting the trend of the change we smoothed the curves and get the frequency variation of the Hx component in the five stations. The basic conclusions are as follows:

1. The peak frequencies are different in different stations, shows the law that the peak frequencies of stations located in high-latitude are larger than the stations in low-latitude.
2. The variation of the peak frequencies have obvious and synchronous annual variation characteristics in the first four SR mode. The fundamental mode shows the sinusoidal periodic and the second harmonic mode shows the half- sinusoidal periodic while the feature of the first and the third harmonic is the superposition of sinusoidal and half- sinusoidal periodic. The other harmonic mode behaved their own rules but lack of synchronism between different stations

**Keywords:** Schumann Resonance, frequency shift, annual variation

# On separation of *Sq* field and EM response estimation using seafloor array data

Kiyoshi. Baba[1]
[1]Earthquake Research Institute, The university of Tokyo

**SUMMARY**

For estimation of electromagnetic (EM) response functions at the periods between $10^4$ and $10^5$ seconds from seafloor magnetotelluric data, the effects of complex external source fields (e.g., geomagnetic solar quiet daily variations (*Sq*) and tides) are necessary to take into account. One of the ways to deal with this problem is to determine the amplitude and phase of time variation for known periods of *Sq* and tides and to subtract them from the observed data (detiding). However, the reduction of the effects is not enough to obtain reliable EM responses (Shimizu et al., 2011). In this study, I first revisit the impact of detiding on EM response estimation. The reduction of the line spectra was improved if the annual variations of the amplitude of these variations, which is manifested as line spectra at both sides close to the periods, are considered. However, the resultant EM responses still show unrealistic feature. I then applied independent component analysis (ICA) to separate *Sq* field from the observed magnetic data. *Sq* field is based on the current in the ionosphere, which is excited by heating of neutral atmosphere by Sun. Then, I may suppose that the simplest instantaneous mixing model can be applied by treating the data with local time of each station. Applications of the ICA to real seafloor array data seems that it was succeeded qualitatively to detect *Sq* like components by investigating the detailed time variation and power spectrum of each independent component and correlations of mixing coefficients to longitude and latitude. Quantitative evaluation of the independent components is necessary to study farther for establishing the method applicable to general data.

**Keywords:** marine magnetotellurics, Sq, EM response estimation, detide, independent component analysis

# Possibilities for processing TEM data with quality check: *TEM-Processing* software

M. Sharlov[1], Yu. Agafonov[2], I. Bouddo[3]
[1] SIGMA-GEO Ltd., Institute of the Earth's Crust of the Siberian Branch of the RAS, sharlov@sigma-geo.ru
[2] SIGMA-GEO Ltd., Institute of the Earth's Crust of the Siberian Branch of the RAS, agafonov@sigma-geo.ru
[3] SIGMA-GEO Ltd., Institute of the Earth's Crust of the Siberian Branch of the RAS, biv@sigma-geo.ru

## SUMMARY

The *TEM-Processing* software is designed to process full-waveform data of transient electromagnetic surveys. The software, with its built-in options of data analysis and visualization, is a powerful tool for studying transient responses. The settable workflow includes several steps: low-pass filtering, stacking, interpolation to log time grid, time shifting, and final stacking. The algorithms that ensure the highest processing quality are specified by the user or chosen automatically at each step. Statistical quality parameters are calculated at all steps, including the total value for each resulting curve. The program processes most soundings automatically and highlights those that require user's attention.

**Keywords:** TEM, transients, data processing, quality check, curves

## INTRODUCTION

Transient electromagnetic (TEM) soundings are used broadly to detect aquifers, mineralization and permafrost within the shallow subsurface, as well as oil and gas accumulations at greater depths. The surveys can cover hundreds of square kilometers, at a density of 30-40 points per square km (Sharlov et al., 2017).

Most TEM soundings acquired in Russia are measured and recorded with *FastSnap* or *SGS-TEM* digital multichannel telemetric systems (for shallow and deep applications, respectively). Both systems record full-waveform signals (sampled on an arithmetic grid) and save data in the SGS format to a database for further processing. A similar approach was previously used in the LOTEM system (Strack et al., 1989). This method has better noise immunity than obtaining TEM curves directly at the sounding points by stacking in time windows, without saving raw data. However, the signals sampled and stored in this way make up huge datasets of transients to be processed.

Data processing includes rejection, filtering, and averaging of raw data for different operation modes and their final stacking into the resulting voltage decay curve. Standard stacks at each point may comprise 1500 – 3000 pulses (digitized individual EMF decays). Especially for large datasets (exceeding a few hundreds of measurements) automatic processing would yield significant savings on labor costs. The *TEM-Processing* software allows automatic processing of SGS data.

## SGS DATA FORMAT AND PROCESSING SEQUENCE

The SGS format is a combination of attribute data stored in the relation database and raw data files in the binary form. The attribute data include the measured parameters of each signal (transmitter current, gain, sampling rate, etc.) and a link to the binary data file. The data file contains a set of individual pulses consisting of full-waveform ADC samples.

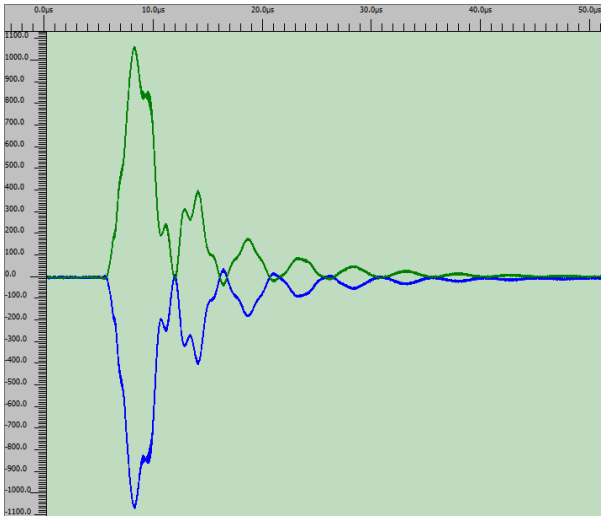


**Figure 1.** One hundred bi-polar pulses (content of one record) are displayed on a single time scale. Voltage decay is affected by high-frequency noise ("ringing" of TX and RX loops).

Thus, data of each sounding are stacks of elementary pulses recorded with the same system settings. As a rule, each record comprises 100 –

200 pulses (Figure 1) with 15 to 30 such records per point (depending on noise).

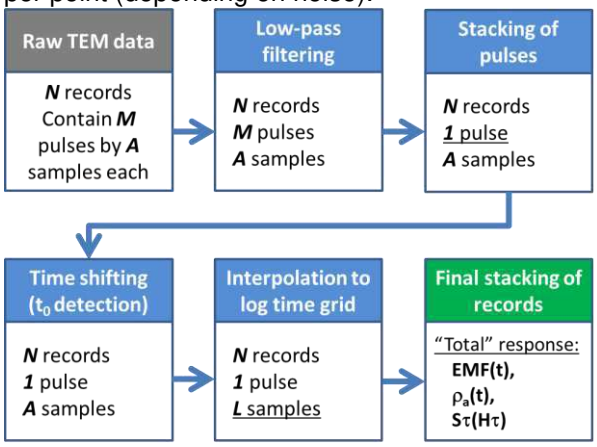


**Figure 2.** Processing flow.

The structure and content of the raw data determine the processing time. Depending on the chosen settings, the processing algorithm may consist of several successive steps (Figure 2). The steps change the content of the data and some steps also reduce data volume. The steps are detailed below.

**Low-pass filtering**

Full-waveform transients may be affected by aperiodic (random) or periodic (harmonic) noise from broadcasting, power lines, loop ringing, etc. (Figure 1), or their combinations. Simple statistical stacking can suppress random noise but is inefficient in the case of harmonic noise which requires a separate procedure of low-pass filtering. A frequency analyzer picks noise in the signal spectra and filters low-frequency noise automatically. The filtering algorithm parameters (frequency range, number of iterations for noise picking, number of frequencies, noise amplitude, etc.) are specified by the user and impose limits on the extent of processing.

**Averaging / stacking**

The measured TEM responses cover a large dynamic range (up to 180 dB), and statistical stacking is indispensable for late time responses. Thus, the stacking /averaging step aims at noise attenuation and increasing the signal-to-noise (S/N) ratio in each sample. The averaging procedure converts the set of ***M*** raw pulses, each consisting of ***A*** samples, into a single averaged pulse likewise including ***A*** samples (Figure 2). *TEM-Processing* implements several averaging algorithms for different noise conditions: robust procedures (Huber M-estimator, median) stable to random noise and those based on arithmetic mean (trimmed mean, weight summation, etc.) for less complicated noise conditions which, however, provide estimates closer to the mathematical expectation. The optimal procedure for a given dataset is chosen according to S/N ratios.

**Time shifting ($t_0$ placing)**

The resulting TEM curve is obtained by combining segments of the curve (Sharlov et al., 2017) acquired with different settings and transmitter currents (which affects the turn-off duration).

Joint processing of curves collected at different transmitter currents requires time shifting to place the record origin $\mathbf{t_0}$ at the time when the transmitter current is off. The time shifts required for data acquired at low current, with the shortest turn-off time, are usually determined based on the transmitter loop size and, to some extent, on the shallow earth conductivity. In other acquisition conditions, time shifts are chosen automatically by the least square method. Thus, the time shifting procedure ensures the best consistency of curves in time prior to final stacking (Figure 3).

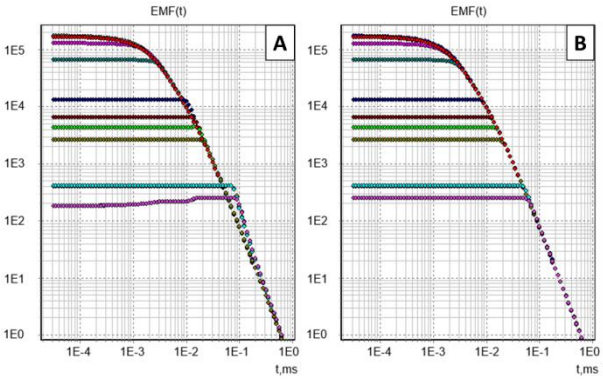


**Figure 3.** Voltage decay curves EMF(t), with different system settings shown in different colors, before (A) and after (B) time shifting.

**Interpolation to log time grid**

In their final form, the transients and their transformations are calculated on a log time grid, due to the mathematical properties of the curve shape: a smooth function decaying slowly at late times. Therefore, the series of raw full-waveform samples is converted to a log-grid series by interpolation. *TEM-Processing* can run linear, spline, polynomial, and windowing interpolation procedures. Some procedures correspond to Hamming (1977) low-pass filtering (e.g., binomial interpolation) and additionally improve the S/N ratio of each output sample.

**Final stacking**

The interpolated voltage decay curves are loaded into the module of final stacking to obtain the resulting curve that covers the full range of soundings in all modes. All data are stacked using a single averaging algorithm. The time ranges suitable for stacking are selected for each curve while the intervals of ADC overload ("clipping") and

late-time low S/N are excluded. Thus, only the intervals that contain good signals are used for final stacking thus providing the best possible quality of the resulting curve which is saved to the database. It is saved together with processing parameters, including low-pass filtering settings, to be used further in inversion for reducing early-time error (Sharlov, 2017).

**Quality check**

The raw full-waveform data used for final stacking allow calculating statistical parameters of data quality: S/N ratios for each sample and averaging error $\mathbf{E_m}$ referring to statistical stacking at each sample (Guseinov et al., 2015). These criteria provide reliable quality checks for the resulting curves and are used to automatically limit the late-time to the interval of satisfactory quality. The quality parameters are saved to the database together with the resulting curve and provide an estimation of its quality. The quality parameters are used further in inversion.

## AUTOMATIC DATA PROCESSING

The option of automatic processing is especially useful to handle hundreds and thousands of soundings. Run in this mode, *TEM-processing* operates with all loaded data, and the workflow can be specified by the user. The program automatically loads the data for each sounding, analyzes them, runs the specified steps, and yields the final curve and its quality estimates. The curves of high quality are saved to the database automatically, while those of inferior quality, unfit for automatic saving, are marked by color (Figure 4 on the Page 4) to highlight the data to be processed by the user. According to our experience, manual processing is needed for no more than 15-20 % of all curves.

## CONCLUSIONS

The *TEM-Processing* software has a flexibly settable algorithm that can cope with both random and periodic noise and yield a high-quality resulting curve of voltage decay. Estimation of quality parameters for each curve, on the basis of representative raw data statistics, provides reliable quality checks. The program features an option for automatic processing, especially useful to process large numbers of soundings. It applies automatic quality checks and highlights data that require special user's attention.

## REFERENCES

Guseinov, R.G., Petrov, A.V., Agafonov, Yu.A., Sharlov, M.V., Buddo, I.V., Gomulsky, V.V. (2015) A quality check system for TEM surveys. Vestnik IrGTU, 100 (5), 53-60.

Hamming R.W. (1977) Digital Filters. Prentice Hall, 226 pp.

Sharlov, M.V., 2017. Integrated approach to processing and inversion of shallow TEM data: Evaluation of efficiency according to modeling results, in: Engineering Geophysics-2017. Extended Abstracts, 13-th Conf. and Exhibition, Kislovodsk.

Sharlov, M.V., Buddo, I.V., Misyurkeeva, N.V., Shelokhov, I.A., Agafonov, Yu.A. (2017) Experience of efficient near-surface studies by the shallow TEM method using the Fastsnap system. Pribory i Sistemy Razvedochnoi Geofiziki 38 (2), 8 – 23.

Sharlov, M.V., Buddo, I.V., Misyurkeeva, N.V., Shelokhov, I.A., Agafonov, Yu.A. (2017). Transient Electromagnetic Surveys for High-Resolution Near-Surface Exploration: Basics and Case Studies. FirstBreak, 35, September 2017, 63 – 71.

Strack, K.-M., Hanstein, T.H., Eilenz, H.N. (1989) LOTEM data processing for areas with high cultural noise levels. Physics of the Earth and Planetary Interiors, 53, 261—269.

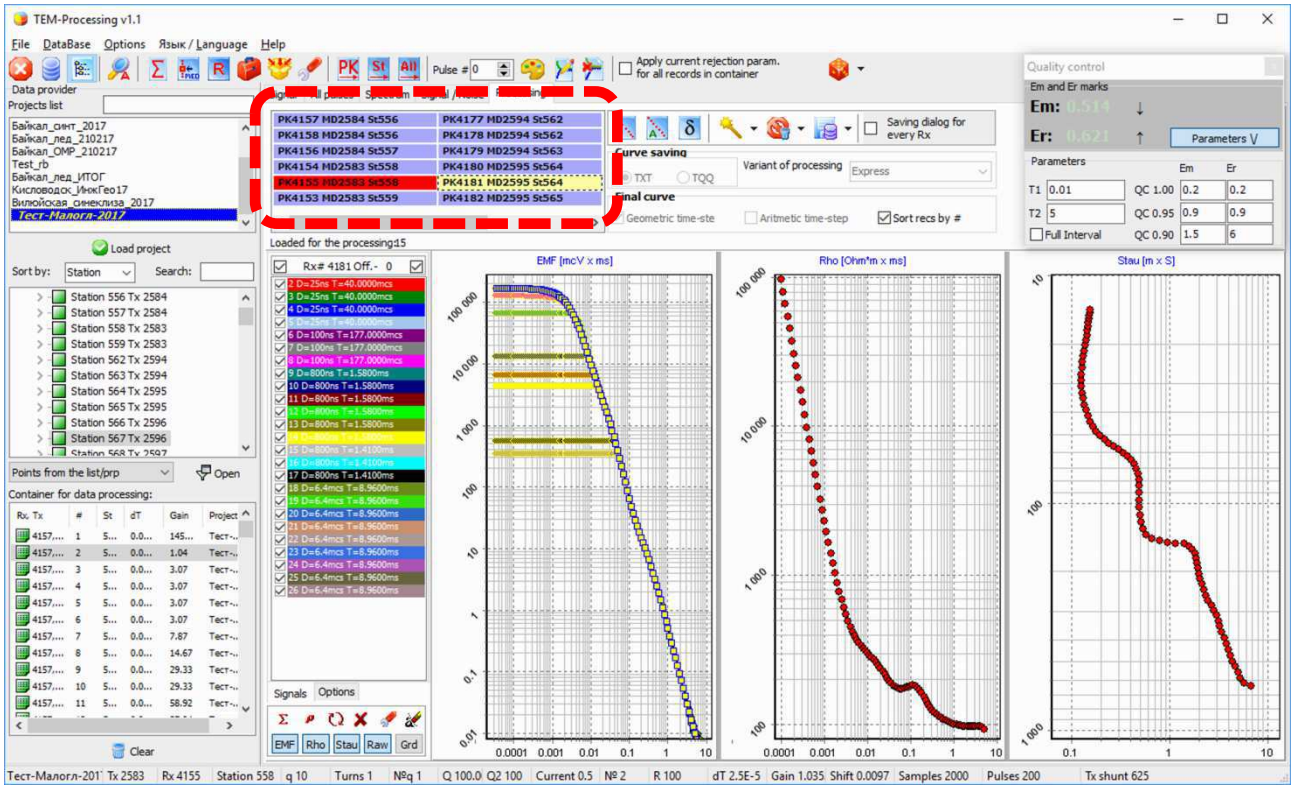


**Figure 4.** Automatic processing of shallow TEM data, each sounding point is displayed with different colors showing quality parameters of curves (blue for satisfactory quality, yellow for good quality, red for data that require manual processing).

# Processing of semi-airborne EM data in the framework of the DESMEX project

M. Becken[1], M. Schiffler[2], C. G. Nittinger[1], M. Cherevatova[1], A. Steuer[3], T. Martin[3], U. Meyer[3], W. Moerbe[4], P. Yogeshwar[4], B. Tezkan[4], R. Rochlitz[6], T. Günther[6], B. Friedrichs[8], U. Matzander[8] , V. Zakosarenko[7], R. Stolz[2] and the DESMEX project group[1,2,3,4,5,6,7,8]

[1]Institute of Geophysics, University of Münster, Germany, michael.becken@uni-muenster.de
[2]Leibniz-Institute for Photonic Technology (Leibniz-IPHT), Jena, Germany
[3]Federal Institute for Geosciences and Resources (BGR), Hannover, Germany
[4]Institute of Geophysics and Meteorology, University of Cologne, Germany
[5]Institute for Mineralogy, Technical University Freiberg, Germany
[6]Leibniz-Institute of Applied Geophysics (LIAG), Hannover, Germany
[7]Supracon AG, Jena, Germany
[8]Metronix GmbH, Braunschweig, Germany

**SUMMARY**

In the DESMEX project, we develop technologies and methods for airborne measurements of the electromagnetic (EM) field generated by a controlled source installed on the ground. The concept is denoted as the semi-airborne method; it has the potential to penetrate deeper than classical airborne EM surveys and to achieve superior spatial coverage than classical ground surveys. Therefore, it can create significant impact for applications in mineral exploration. In this contribution, we report on data acquired during test flights with two novel helicopter-towed bird systems. The first instrument combines tri-axial Metronix induction coils with a three-component fluxgate magnetometer, an optically pumped potassium total field magnetometer and an inertial measurement unit (IMU) on one sensor platform. The second bird contains an advanced vector magnetometer based on three orthogonal SQUID (Superconducting Quantum Interference Device) magnetometers with a low intrinsic noise of about $5fT_{RMS}/\sqrt{(Hz)}$ and a large dynamic range of >30bit, a three-component fluxgate instrument and a data acquisition system encompassing a high-resolution IMU. High-power grounded electric dipoles from the University of Cologne (LOTEM transmitter) and LIAG (High-power "DC" transmitter) were employed in these tests. We used dipole moments of up to 40 kA and fundamental injection frequencies of 7.5 Hz and 10.4 Hz, respectively. The area that can be covered in one flight is in the order of 3 km x 6 km centered at the transmitter locations.

The processing consists of estimating linear transfer functions between the injection current and the recorded vectorial EM field components in frequency domain. The dominant noise source in the data is due to motion of the system in the Earth's magnetic field. Removal of motion noise is therefore a crucial step in data processing. The IMU installed within the bird records the attitude of the system with an accuracy of 0.01° and a sampling rate exceeding 400 Hz. Motional noise with frequencies higher than recorded by the IMU (i.e. vibrations) cannot be corrected for but are expected to be of minor influence. Motion can cause i) projection errors given that the sensor orthogonality is granted to within 0.1° only ii) motional induced voltages, when the sensor measures the flux change with time and iii) heading errors due to magnetized parts, ferromagnetic parts and induced eddy currents in conductive parts of the bird.

We present processing schemes for all sensor types that can (partially) compensate for motional effects and that yield reliable total magnetic intensities as well as transfer functions between the vector components and the injection current. We also propose to evaluate frequency-domain transfer functions from the spectrum of the total field. This estimate is theoretically superior in terms of motional noise elimination and effectively estimates the transfer function in the direction of the main field. Overall, we can semi-airborne EM transfer functions for frequencies in the range from 10 Hz to 5 kHz from data recorded during one flight and with accuracies of better than 5-10 pT/A.

**Keywords:** semi-airborne EM, motion noise, mineral exploration

# Quality Characterization of Long Term Magnetometer Array Data using Feature Extraction and Classification

K. Kappler[1], T. Bleier[1] , L. MacLean[1] and D. Schneider[1]
[1]QuakeFinder, kkappler@quakefinder.com

**SUMMARY**

Since 2005 QuakeFinder (QF) has acquired via a distributed array of remote measuring stations, a unique dataset with outstanding spatial and temporal sampling of earth's magnetic field variations along several active fault systems. This network consists of 124 stations in California and an additional 45 stations along fault zones in Greece, Taiwan, Peru, Chile and Indonesia. Each station is equipped with three feedback induction magnetometers continuously recorded at 50Hz with GPS timing. A 24h segment of data from these sensors from an arbitrary but fixed QF station we refer to a "station day". We have acquired approxiamtely 300,000 station days to date. QF is attempting to detect and characterize anomalous EM activity occurring ahead of earthquakes. Here we provides a status report of our effort.

Previously we reported on an algorithm which flags candidate magnetic variations from time series datasets, counts the number of these magnetic field pulses seen at each station on each day, and ranks each station-day according to the aggregate number of pulses in a time window preceding the day in question. If previous suppositions are true that there is more magnetic field activity preceding an earthquake over some time interval, this should reveal itself by the station-days on which earthquakes occur being ranked higher on the list than they would be if the ranking scheme were random. This hypothesis can be validated by using the Receiver Operating Characteristic (ROC) test.

Previously we deployed the algorithm on a dataset comprising approximately 20,000 station days and found greater than two standard deviations statistical significance. However, when we scaled the dataset from 100-day time intervals before quakes, which had been Quality-Control (QC) reviewed at least to first order by human eye to long term analysis we discovered inconsistent results. This led us to further QC our time series using several tools including remote reference station transfer function analysis, and median daily variances of windowed time series. These calibrated views of the data when applied over decade long series revealed clear step changes in the data character, corresponding to instrument or station configuration changes, as well as occasionally changes in the ambient noise environment. Over the long term these step changes comprise the dominant features of most station time series making it impractical to see more subtle changes possibly associated with earthquakes. We review the procedures used to normalize the data and discuss other considerations with long term analysis, such as statistical compensation for the effect of smaller close earthquakes as compared with large further quakes for a given station. Finally we compare baseline significance with and without calibration and discuss the implications for processing QF and other long term array data.

**Keywords:** QC, Signal Processing, Transfer Functions, Time Series, Magnetics

# Source Biases in Magnetotelluric Transfer Functions due to Pc3/4 (~10-100s) Geomagnetic Pulsations at Mid-Latitudes

Benjamin S. Murphy[1] and Gary D. Egbert
College of Earth, Ocean, and Atmospheric Sciences; Oregon State University; Corvallis, Oregon, USA
[1]murphybe@oregonstate.edu

**SUMMARY**

Discussion of possible bias in magnetotelluric (MT) transfer functions due to the finite spatial scale of external source fields has largely focused on long periods (>1000 s), where skin depths are large, and high latitudes (>60° N), where sources are dominated by narrow electrojets. However, a significant fraction (~15%) of the ~1000 EarthScope USArray apparent resistivity and phase curves exhibit nonphysical "humps" over a narrow period range (typically between 25-60 s) that are suggestive of narrow-band source effects. Maps of locations in the US where these biases are seen support this conclusion: they mostly occur in places where the Earth is highly resistive, such as cratonic regions, where skin depths are largest and hence where susceptibility to bias from short-wavelength sources would be greatest. We have analyzed EarthScope MT time series using cross-phase techniques developed in the space physics community to measure the period of local field line resonances associated with geomagnetic pulsations (Pc's). In most cases the biases occur near the periods of field line resonance determined from this analysis, suggesting that at mid-latitude (~30°-50° N) Pc's can bias the time-averaged MT transfer functions. Because Pc's have short meridional wavelengths (hundreds of km), even at these relatively short periods the plane-wave assumption of the MT technique may be violated, at least in resistive domains with large skin depths. It is unclear if these biases (generally small) are problematic for MT data inversion, but their presence in the transfer functions is already a useful zeroth-order indicator of resistive regions of the Earth.

**Keywords:** source bias, geomagnetic pulsations

# Temporal changes of geomagnetic induction arrows in non-seismic regions: fiction or reality?

T. Ernst[1] and W. Jóźwiak[1]
[1]Institte of Geophysics, Polish academy of Sciences, ks. Janusza 64, 01-452 Warsaw, Poland

**ABSTRACT**

Various scientific articles report that induction arrows estimated in the same place are changing over the time, which should not happen in seismically non-active regions. The induction arrows in geomagnetic sounding are strictly related to local deep conductivity distribution (geological structure). In general, the geological structure is stable in non-seismic areas.
So, in our opinion, the temporal changes of induction arrows signaled in the literature, are related to the estimation errors produced in calculation process by the presence of the external part of vertical field, appearing as noise in the data set. And additionally, what is very important, this noise is correlated with input signals.
To confirm our thesis, we estimated induction arrows at different time periods (seasons), analyzing carefully their variability. For calculations we used one-minute recordings of geomagnetic variations from some magnetic observatories and selected permanent sites in Poland and Lithuania registered between 2002-2015.
In data processing we used an algorithm based on the method of least squares in the time domain. Our task is a typical problem of studying a linear system (black box) of two input signals (horizontal components of geomagnetic field) and one output signal (induction part of the vertical field). Unfortunately, assumption that the external sources are spatially uniform, is often not satisfying, and the external part of the vertical field usually exists, and sometimes is much bigger than the internal part.
The impulse responses obtained in the calculation process allowed us to easily predict the induction (internal) part of the vertical magnetic field by the convolution of such responses with the variations of two horizontal components. And then, in the next step we were able to separate the total vertical field into the induction part and the external one, which allows to calculate correctly the induction arrows. Such a prediction in the time domain is more accurate and much easier to make than in the frequency domain and, most importantly, it can be calculated on line.
The results demonstrate, that induction arrows calculated in this way are stable over the time.

**Keywords:** induction arrows, prediction, magnetotellurics

# UAS based magnetic and electromagnetic surveys: Case Studies from mineral exploration and geotechnical projects

J.B.Stoll[1]
[1]An der Riebeck 31, 29223 Celle

**SUMMARY**

Autonomously operated Unmanned Aerial Systems (UAS) are manifesting the acquisition of low cost, high definition geoscience data readily applicable to resource exploration, environmental site characterization, and geotechnical projects as well as ensuring the profitability of resource extraction. The availability of robust, low-to-moderate cost UAS has amplified the interest in utilizing airborne robotic technology in many market sectors.

The big push in the use of drones in the last decade was driven by the increased reliability, portability, decreased costs, smaller and lighter sensors, and promulgated changes in the regulations governing the use of unmanned aircraft in the national air space of many countries.

Within the realm of exploration geophysics, low altitude aeromagnetic surveys conducted with an UAS is emerging as a viable cost-effective alternative to ground magnetic surveys. The motivation to deploy an UAS platform fitted with a magnetometer stems from the inherent ability of the aircraft to fly at low and ultra-low altitudes with minimum risk to the field personnel and property.

In this presentation results of aeromagnetic surveys with both a 5kg hexakopter and a 5 kg fixed wing UAV are presented. These are examples from surveys over an iron ore deposit, as well as operations over UXO contaminated areas and over a gas pipeline.

Radio frequency electromagnetic system operating in the very low frequency (VLF) and low frequency (LF) range has been developed for use on an unmanned helicopter. Much effort was undertaken to reduce the weight and optimize the performance of existing geophysical instruments for the use on a drone.

Two example surveys over gas pipeline are presented, which demonstrate the applicability of RadioEM to locate and track highly conductive structures.

All projects show that the use of UAS in geophysics increases productivity by at least a factor of 10 compared to measurements on the ground. The mobilization costs compared to conventional airborne geophysics with manned aircraft are negligible. The data are higher resolution and enjoy a greater spatial density than data acquired with conventional ground and airborne methods.

**Keywords:** 5 kg Hexacopter, fluxgate sensor, RadioElectromagnetics,

# Weak signal processing technology of low frequency GPR based on Hilbert-Huang transform and its application in permafrost area gas hydrate exploration

Bai Dawei[1], Qiu Gengen[2] and Fang Hui[3]
[1] Institute of Geophysical and Geochemical Exploration, baidawei@igge.cn
[2] Institute of Geophysical and Geochemical Exploration, qiugengen@igge.cn
[3] Institute of Geophysical and Geochemical Exploration, fanghui@igge.cn

## SUMMARY

As the low frequency ground penetrating radar acquisition time window is large, the deep strata affected by signal attenuation and dispersion is very obvious, the real reflection signals are often accompanied by a lot of noise, so the low frequency GPR signal can be regarded as the typical non-stationary signal. We use the Hilbert-Huang transform method, which is very good in non steady signal processing, to study the weak signal processing method. It can effectively filter the abrupt change part and noise in the signal, so as to detect and extract the deep weak signal. Using this method to explore the gas hydrate in permafrost zone, the effective reflection signal of low frequency ground penetrating radar signals in the bottom of permafrost and its natural gas hydrate reservoir can be extracted, and good results are obtained.

**Keywords:** Low frequency ground penetrating radar; Hilbert-Huang transform; weak signal processing; gas hydrate in permafrost area

## INTRODUCTION

Ground penetrating radar (GPR) is a geophysical method using high frequency electromagnetic waves (frequency range generally between 1MHz-4GHz) for underground exploration. This method is used to transmit high frequency electromagnetic waves through a transmitting antenna to receive an antenna to receive electromagnetic waves reflected back to the ground, and the electromagnetic wave has an electrical difference when it propagates in the subsurface medium. A reflection occurs at the interface, and the information of the spatial position, structure, shape and buried depth of the underground medium is infer based on the changes in the waveform, amplitude, and time of the electromagnetic wave. Low frequency ground penetrating radar (GPR) usually refers to ground penetrating radar with frequency range between 1-50MHz. The depth of detection is greater than that of conventional GPR, and can reach more than 100-200 meters in some specific environments. In China, the buried depth of natural gas hydrate reservoirs in the continental permafrost region is within 200 meters, which makes it possible to use low frequency ground penetrating radar to detect natural gas hydrate directly. In order to achieve relatively deep detection depth, the low frequency ground penetrating radar system adopts a larger time window (generally above 2000ns), large size antenna and long distance transmission distance. It is difficult to use the shielding device as high frequency GPR to suppress the noise, so the low frequency GPR signal is disturbed by the more energy echo of the air, and the echo of the deep reflection layer is weak. It can be regarded as a typical nonstationary and nonlinear signal. For non-stationary and nonlinear signals, the more intuitive analysis method is to use parameters with local characteristics such as instantaneous frequency and instantaneous phase. Hilbert transform is often used to solve the instantaneous frequency and instantaneous phase characteristics of the signal, but many signals may appear unexplained and lack of actual physical meaning after Hilbert transform. After studying the instantaneous frequency deeply, Norden E. Huang proposed a new time-frequency analysis method -- Hilbert-Huang Transform (HHT). HHT consists of two key steps: Empirical Mode Decomposition (EMD) and Hilbert spectrum analysis. EMD decomposes the signal into a series of eigenmode functions (Intrinsic Mode Function, IMF), which makes the instantaneous frequency of the Hilbert transformation of each IMF has a certain physical meaning, and thus can be more accurate and effective in analyzing the characteristic information of the signal.

Based on the HHT method, this paper studies the low frequency GPR deep weak signal extraction technology, and carries out HHT transform to the original data of low frequency GPR, and can obtain the corresponding instantaneous attribute information of each order IMF, thus effectively distinguishing the reflection signal and noise of the formation. The technology can be applied to the exploration of natural gas hydrate in the permafrost

regions of the land, and it can effectively distinguish the natural gas hydrate reservoir of the bottom boundary of the permafrost and its underlying distribution.

## DATA ACQUISITION AND

In July 2016, a low frequency GPR test was carried out nearby the DK9 well, which had been obtained gas hydrate samples in the Qinghai area. A total of two lines were set up (Figure 1), of which the Line1 was 600 meters long and the Line2 was 600 meters long. The instrument is a pseudo-random ultra deep GPR system developed by the Institute of electronics, Chinese Academy of Sciences. The specific parameters are shown in Table 1.

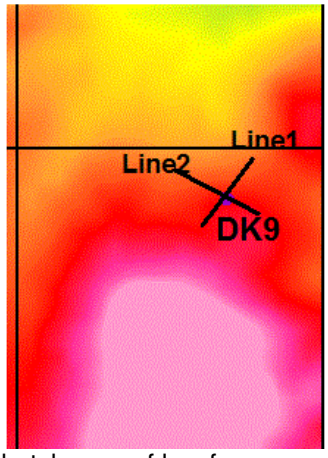


Figure 1 sketch map of low frequency GPR test section

Table 1 main parameters of low frequency ground penetrating radar

| Parameter | value |
|---|---|
| Encoding method | 8192 sets of Golay coding |
| Code width | 80 ns |
| Phase encoding length of each group | 8 |
| Emission peak power | 1kW |
| Receiver sensitivity (including pulse compression) | -130dBm |
| Mixed sampling interval | 5ns |
| Gain range of time-varying gain circuit | -10~53dB |
| Linear mean times | 1/2/4/8/16 |
| Emission center frequency | 12.5MHz |
| Pulse repetition frequency | 200KHz |
| Antenna form | 12.5 meter long resistance loaded dipole antenna |
| Maximum detection window | 4200ns |

## ANALYSIS

The processing methods and results of Line2 line are mainly introduced here. First, single channel analysis is performed: the HHT transform of single channel data at DK9 well is performed to get the IMF components of each order and their instantaneous spectrum(Figure 2). In Figure 2 (A), the DATA curve is the original signal waveform, IMF1-5 is the IMF component curve of each order, and R is the residual value. The blue curve above in Figure 2 (B) is the original data. The red block is the location of the gas hydrate reservoir. It can be seen that the amplitude intensity of the original data is not obvious, which is caused by the weak reflection of the deep signal and the strong geological noise. On the IMF1 and IMF2 component curves, gas hydrate reservoirs are reflected to different degrees (IMF1 is better). From the corresponding instantaneous frequency component distribution, it can be seen that there is a obvious frequency mutation above the gas hydrate reservoir, which is rapidly reduced from high frequency oscillation to the normal range. Through the spectrum analysis of the original data, the general gas hydrate reservoir range can be quickly and visually delineated.

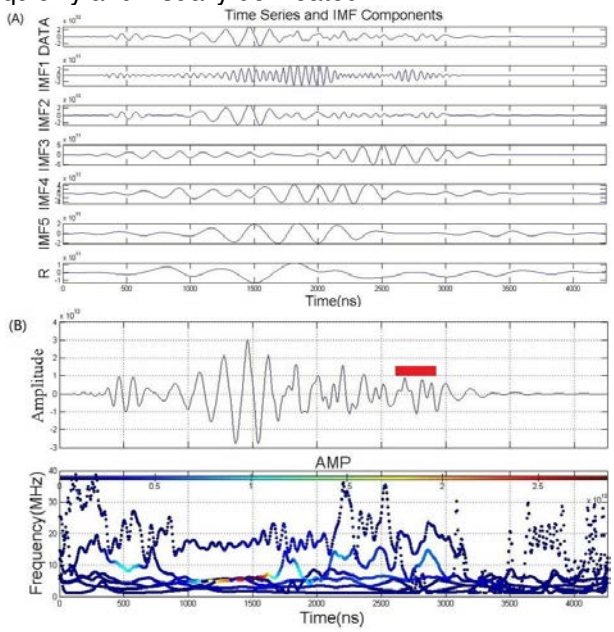


Fig. 2 IMF component (A) and instantaneous energy spectrum of single channel GPR original signal at DK9 (B)

After superposition of IMF1 IMF2, the signal is reconstructed and the single channel signal with higher signal to noise ratio is obtained. It has a good correspondence with the logging resistivity curve, core information and hydrate reservoir in DK9 (Figure 3). According to the logging data, it is determined that about 120 meters at the bottom of the permanent frozen soil layer. From the GPR image we can see that there is a significant amplitude and frequency change in the signal. The layer of 180-200 meters is the rock layer of the discovery of the hydrates, and the amplitude and frequency change on the GPR signal. Based on the results, a 2D GPR section interpretation map was obtained (Figure 4).

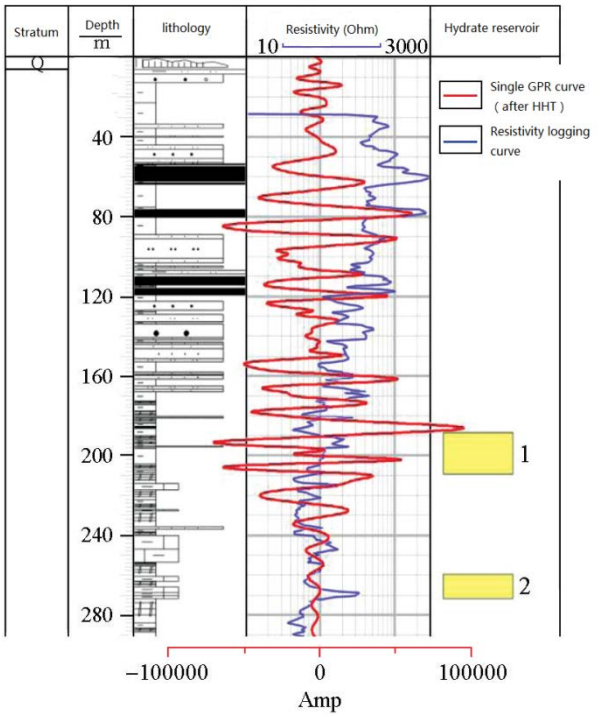


Fig. 3 Comparison of GPR signal and logging apparent resistivity at DK9

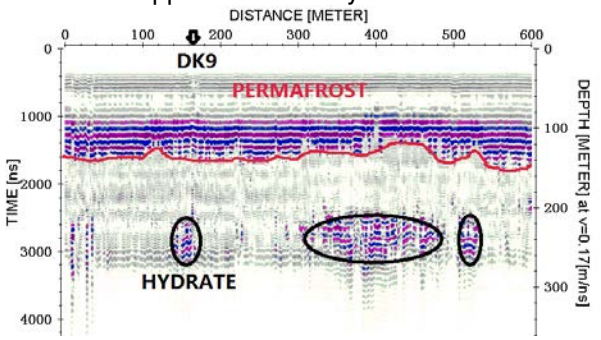


Fig. 4 2D GPR profile interpretation (above the red line is the permafrost, the hydrate layer and the suspected hydrate layer in the black circle).

## CONCLUSIONS

(1) The time window of the low frequency ground penetrating radar is large, the deep signal is greatly influenced by the attenuation and dispersion of the ground. The real reflection signals often accompany a lot of noise, so the low frequency ground penetrating radar signal can be regarded as a typical non steady state signal. On the basis of the Hilbert-Huang transform method, the processing method of weak signal of low frequency GPR is studied.

(2) The low frequency GPR detection technology based on the HHT processing method can be used to directly detect the permafrost bottom boundary and the gas hydrate reservoir in the continental permafrost area.

## ACKNOWLEDGEMENTS

This study is supported by the national high technology development plan "863 Plan" (2012AA061403); the national 127 special project (GZHL20110324;GZH201400305); Geological survey project of China Geological Survey (DD20160224); Special fund for basic research and business expenses of central public welfare research institutes (AS2015P02;AS2014J09)

## REFERENCES

Norden E. Huang, M. L. Wu, S. R. Long, et al. A confidence limit for the Empirical Mode Decomposition and Hilbert Spectral Analysis. Proceedings Royal Society of London, 2003, A459, 2,317-2,345.

Wu, Z. and N. E. Huang. A study of the characteristics of white noise using the empirical mode decomposition method, Proceedings Royal Society of London, 2004, A460, 1597-1611.

# Why Do EM Data Pervasively Follow a Stable Distribution?

Alan D Chave[1], David J Thomson[2] and Douglas S Luther[3]
[1]Woods Hole Oceanographic Institution, MA, USA, achave@whoi.edu
[2]Queens University, Ontario, Canada, djt@queensu.ca
[3]University of Hawaii, HI, USA, dluther@hawaii.edu

## SUMMARY

This paper describes the analysis of geomagnetic variations from Honolulu Observatory over the frequency band 250-5000 μHz for the presence of narrow (<2 μHz bandwidth) spectral peaks and nonstationarity, as evidenced by correlation between frequencies in the same data. These phenomena are ubiquitous over the entire frequency band, and correlate well with the frequencies and Qs of normal modes of Sun. Nonstationarity in the presence of forcing at a given frequency leads to the nonlinear transfer of power to other frequencies, and ensuing non-Gaussian statistics, that is very strong in these data. By comparison with a contemporaneous seafloor pressure record, it is postulated that solar modes impact the bow shock over a wide area and literally shake Earth by exerting a torque on the geomagnetic field, which then couples into the solid earth and ocean. Finally, it is argued that the pervasive stable law behavior of geomagnetic variations in the frequency domain is the consequence of the strong, observed nonlinearity, and hence non-Gaussianity, driven by widespread nonstationarity from solar normal mode forcing.

**Keywords:** nonstationary, non-Gaussian, stable distribution, geomagnetic variations

## INTRODUCTION

Thomson et al. (2001, 2007) and Thomson and Vernon (2015, 2016) presented a comprehensive analysis of a wide range of terrestrial data, including seismic, geomagnetic, barometric and interplanetary ones, that show that their spectra at frequencies above ~250 μHz are dominated by narrowband, high-Q modes whose frequencies and behaviors are consistent with normal modes of Sun. Chave et al. (2018) analyzed seafloor pressure data from the deep ocean near Hawaii, demonstrating the presence of the same type of modes at frequencies up to 4000 μHz. In this paper, contemporaneous geomagnetic data from Honolulu Observatory are evaluated using the same approach as for the pressure data.

Chave (2014, 2017) has shown that frequency domain EM data are pervasively described by the stable distribution family whose tails are algebraic rather than exponential. It is a purpose of this paper to investigate the origin of the stable property.

## METHODS

Assuming a data sequence $x_t$ is from a stationary, harmonizable random process implies a spectral representation (Cramér, 1940)

$$x_t = \int_{-1/2}^{1/2} e^{i2\pi\xi t} dX(\xi) \quad (1)$$

where $\mathcal{E}[dX(f)] = 0$, $\mathcal{E}$ denotes the expected value and $dX(f)$ is an unobservable orthogonal increments process, or a generalized Fourier transform. The true power spectral density $S(f)$ is defined by

$$S(f)\,df = \mathcal{E}\left[|dX(f)|^2\right] \quad (2)$$

The assumption of stationarity requires that the autocovariance sequence be independent of time, implying that

$$\mathcal{E}\left[dX(f_1)\,dX^*(f_2)\right] = S(f_1)\,\delta(f_1 - f_2)\,df_1 df_2 \quad (3)$$

where $\delta(x)$ is the Dirac delta function. In other words, stationarity requires that the spectral density at distinct frequencies be uncorrelated. When the process is non-stationary, (3) is replaced by

$$\mathcal{E}\left[dX(f_1)\,dX^*(f_2)\right] = S_L(f_1, f_2)\,df_1 df_2 \quad (4)$$

where $S_L$ is the Loève spectrum (Loève, 1945). Non-stationarity implies that the spectral density at distinct frequencies will be correlated. In the presence of forcing at a given frequency, this also indicates that power will be redistributed from that point to other frequencies. Since such a power transfer cannot be modeled as a linear process, this means that forced nonstationarity is inherently nonlinear. Further, it is well known that, while linear processes are essentially Gaussian (e.g., Mallows,

1967), nonlinear processes lead to non-Gaussian behavior.

Two tools based on the multitaper spectral estimator will be used in the analyses of this paper: standardized (after removing a quadratic polynomial from log frequency-log power over 200-5000 μHz) power spectra with linear frequency-linear power presentation, and offset coherences, which are the squared coherence between distinct frequencies in the same data set. Both of these are obtained over a 60 d data block using a time-bandwidth of 5 and 9 Slepian tapers, yielding a resolution bandwidth of 1.9 μHz, degrees of freedom of ~18 per frequency and at least 120 dB of sidelobe protection. Linear scale spectra are used because they enable resolution of the bandwidth of spectral features, and are easily assessed for significance because the standard deviation of a multitaper estimate is the noise level divided by the square root of the number of tapers.

## SOLAR MODES

Some types of internal motions of both Earth and Sun are described by normal modes that are characterized using a spherical harmonic expansion indexed by "quantum numbers" $n$, $l$ and $m$. The radial order $n$ gives the number of zeros along a radial line, while the degree $l$ denotes the number of nodal lines in latitude. The azimuthal order $m$ is the number of nodal lines in longitude, with $-l \le m \le l$, and is a consequence of rotation of Earth or Sun. A given normal mode is characterized by its frequency $f$ and quality factor $Q$, with the latter being the ratio of the center frequency to the full bandwidth at half power.

The solar modes of interest in this paper are the pressure or p-modes, which are acoustic standing waves extending from ~250 μHz to the solar cutoff at ~5100 μHz. They are densely packed above ~2000 μHz, with about 100 modes per μHz when rotational splitting is included. P-modes are excited by turbulence in the solar convection zone, so that their amplitudes are random and nonstationary. The $Q$s of p-modes are several thousand, and increase with frequency. As a consequence, a given mode persists for 1−2 months, and the power spectrum of a measurement driven by them is a function of time. In addition, their frequencies can vary by ~1 μHz from their nominal values, as has been shown through optical measurements.

An important characteristic of p-mode production is that about 1/3 of a given area on Sun at a specific time, or of a given time at a specific location on Sun, displays modal activity, with the pattern varying continuously. Further, at about half of solar wind data segments exhibiting a p-mode peak, a statistically significant corresponding peak is present in magnetospheric data. Combining these observations, it is reasonable to expect a given mode to be observed on Earth about 1/6 of the time.

Thomson et al. (2007) demonstrated coherence of geomagnetic field fluctuations with satellite solar wind measurements that exhibit p-mode behavior, so it has previously been established that solar modes are present in the geomagnetic field.

## RESULTS

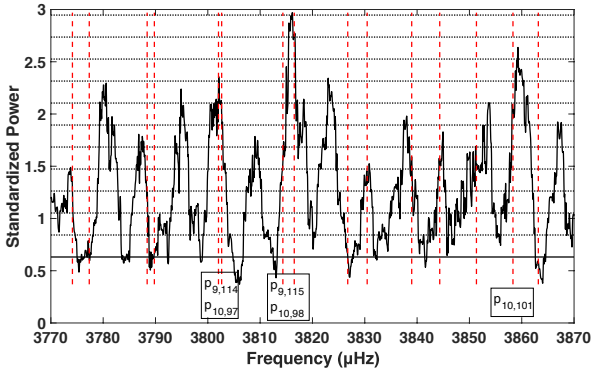


Figure 1. Standardized power for the H component with selected $p_{n,l}$ modes labeled.

Figure 1 shows the standardized power spectrum for the Honolulu geomagnetic north (H) component over the frequency band 3770-3870 μHz (central period of 262 s), which is near the maximum in solar modes at the sun (Christensen-Dalsgaard, 2002). The solid horizontal line shows the estimated noise level taken as the 0.1 power quantile over 3770-3780 μHz, and the horizontal dotted lines show successive increments in standard deviations from that value. The red vertical dashed lines show the nominal center frequencies of solar p-modes from the Michelson Doppler Interferometer without including the rotational splitting terms. Figure 1 shows a set of narrow (2-5 μHz) peaks spaced at 6-10 μHz intervals over the 100 μHz analysis band that are typically at least 6σ, and as much as 11σ, above the noise level. For a Gaussian process such that power is central $X^2$, the probability of a single peak exceeding the 0.1 quantile by 6σ is $2.2 \times 10^{-4}$, and so the probability of independently observing nine such peaks (as in Figure 1) is $\sim 10^{-33}$, which is a reasonable approximation to that of hell freezing over. The conclusion that there is marked non-Gaussianity in these data is inescapable. The spectrum for the vertical (Z) component is very similar to Figure 1, but that for the east (D) component has no resemblance. The pressure spectrum is similar to Figure 1, although the peak heights are smaller. Finally, a 2 μHz wide peak at this frequency implies a Q of at least 2000, which is

commensurate with that of p-modes, but not with any terrestrial phenomenon.

Figure 2 shows the offset coherence corresponding to Figure 1 plotted as center frequency on the abscissa and offset frequency on the ordinate. This quantity is transformed as in Thomson and Vernon (2015) such that values of 1, 2, 3 and 4 in the offset coherence correspond to the 0.9, 0.99, 0.999 and 0.9999 probability levels that two frequencies are correlated, and has been clipped at 4 since the offset coherence at zero offset frequency is always unity. A multitaper offset coherence has the resolution bandwidth on the frequency axis, but has the Rayleigh resolution on the offset frequency axis, accounting for the different behaviors observed in Figure 2.

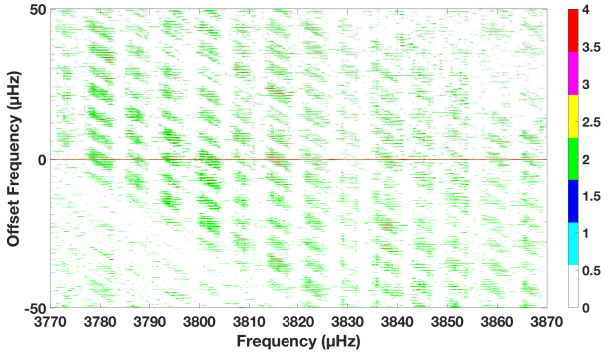


Figure 2. Offset coherence for the Honolulu H component. See text for description.

Figure 2 shows coherence corresponding to correlation probabilities of 0.99 to 0.9999 occurring in symmetric trapezoidal blocks whose frequencies at zero offset correspond to those of the peaks in Figure 1. The trapezoidal shape is not difficult to understand; if frequency $f_1$ is coherent with frequency $f_2 > f_1$, then the coherence will be high at a positive offset frequency $f_2 - f_1$ at frequency $f_1$, and hence at a negative offset frequency $f_1 - f_2$ at frequency $f_2$. Each of the trapezoidal blocks along zero offset frequency have an internal structure that suggests that some of the peaks in Figure 1 comprise numerous narrowband components that are themselves coherent. In fact the spacing of the elongate peaks within each block is approximately the p-mode rotational splitting frequency of ~400 nHz. Trapezoidal blocks also occur at offset frequencies consistent with coherence between the peaks in Figure 1, and certainly extend beyond the ±50 μHz offset frequency range shown. The picture that emerges is one where every peak in Figure 1 is highly coherent both internally and with every other peak, and with additional spectral features beyond the bounds of the figure. This is a manifestation of strongly nonstationary behavior that is consistent with the non-Gaussianity seen in Figure 1.

The vertical magnetic field offset coherence is a slightly less coherent version of Figure 2, while the east magnetic field offset coherence is nearly zero everywhere. Figure 3 shows the offset coherence for the pressure record. The coherence pattern observed in Figure 2 is subdued in Figure 3, but readily identifiable. The results shown in Figures 1-3 are not unusual, and can be seen over other frequency and time intervals commensurate with the observation that modes are observed about 1/6 of the time.

Chave et al. (2018) showed that pressure spectral estimates where modes are present can be fit with a mixture central/non-central $X^2$ model, implying that the data are approximately Gaussian. This is not true for the EM field, as spectral estimates follow a stable power law, and a mixture $X^2$ model fails. Finally, it is not possible to identify which of the peaks in Figure 1 are directly excited by p-modes versus which are the result of non-stationarity because of the high density of p-mode frequencies above 2000 μHz.

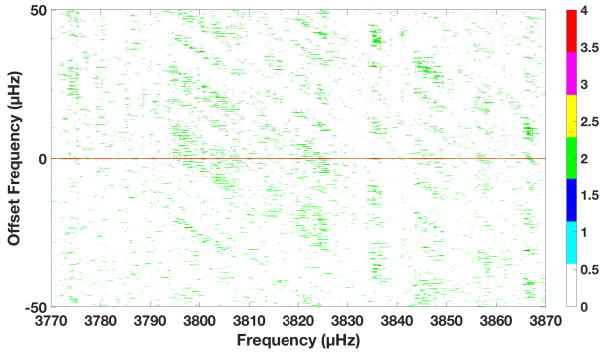


Figure 3. Offset coherence for the seafloor pressure record. See text for description.

## DISCUSSION

Thomson et al. (2007) and Thomson and Vernon (2015) reviewed several models that explain the presence of solar p-modes in terrestrial data. Regardless of the mechanism by which the modes couple into the solar wind, where they are readily observed in satellite data (e.g., Thomson et al., 2001), there are several ways for their presence to reach Earth: 1) irradiance changes in the ultraviolet that modulate the conductivity of the upper atmosphere, 2) bulk flow of the solar wind interacting with the bow shock that changes its equilibrium position, hence coupling into the magnetosphere and 3) fast plasma modes interacting with the interplanetary magnetic field. For the second of these, the modal component will be uniform across the entire bow shock covering ~15 earth radii, resulting in large scale modulation of the magnetic field dominantly in the geographic north direction. Because of the tilt of Earth's rotational axis and the offset between it and the geomagnetic field axis, modes would be expected

to appear predominantly in the north and vertical components of the geomagnetic field. This is exactly what is observed in the offset coherence; the north (H) and vertical (Z) components show persistent and substantial offset coherence while the east (D) component shows very little because of the scale of the forcing. Consequently, the data favor mechanism (2) over the remaining ones.

Further, the amplitude of the modes is much weaker in the seafloor pressure field as compared to the magnetic field. This is apparent in the offset coherence (Figures 2 and 3), in spectra, and in the fact that a mixture central/noncentral $\chi^2$ model fits the pressure data, but not the geomagnetic ones. This militates in favor of a model where solar modes interact with the geomagnetic field, shake the earth by exerting a torque on the geomagnetic field and finally couple from the solid earth into the ocean and atmosphere, with attenuation occurring at each step. Thomson and Vernon (2015) provide energy and torque bounds that demonstrate that this mechanism is quite viable.

Finally, the question posed in the title of this paper needs to be addressed. The geomagnetic field over the solar p-mode band is very nonstationary (e.g. Figure 2) and highly non-Gaussian due to the nonlinear distribution of power from numerous externally forced solar modes to other parts of frequency space (e.g., Figure 1). In fact, it is not possible to tell how far in frequency the nonlinear energy transfer extends, as it is currently impractical to compute the offset coherence over bands longer than a few hundred μHz, but it clearly is far more than a local phenomenon. The persistent nonstationarity and ensuing non-Gaussianity lead to power law rather than exponential tail behavior for geomagnetic variations in the frequency domain, with a stable distribution as the limiting form under the generalized central limit theorem rather than a Gaussian one under the classic central limit theorem. By contrast, nonlinearity in spectra of the seafloor pressure field is much less extensive, leading to a Gaussian model for them.

## CONCLUSIONS

This paper describes the analysis of geomagnetic variations from Honolulu Observatory over the frequency band 250-5000 μHz for the presence of narrow (<2 μHz bandwidth) spectral peaks and nonstationarity, as evidenced by correlation between frequencies in the same data, and their comparison with a contemporaneous seafloor pressure record. These phenomena are ubiquitous over the entire frequency band, and correlate well with the frequencies and Qs of normal modes of Sun. Nonstationarity in the presence of forcing at a given frequency leads to the nonlinear transfer of power to other frequencies, and ensuing non-Gaussian statistics. This effect is much stronger in geomagnetic data as compared to the pressure field. To explain this behavior, it is postulated that solar modes impact the bow shock over a wide area and literally shake Earth by exerting a torque on the geomagnetic field, which then couples into the solid earth, ocean and atmosphere. Finally, it is argued that the pervasive stable law behavior of geomagnetic variations in the frequency domain is the consequence of the strong, observed nonlinearity and non-Gaussianity caused by widespread nonstationarity driven by solar normal modes.

## REFERENCES

Chave, AD (2014) Magnetotelluric data, stable distributions and impropriety: An existential combination. Geophys. J. Int. 198: 622-636.

Chave, AD (2017) Estimation of the magnetotelluric response function: The path from robust estimation to a stable mle. Surv. Geophys. 38: 837-867.

Chave, AD, DS Luther, DJ Thomson (2018) Unexpected high-Q peaks and nonstationarity in the deep ocean infragravity wave band. J. Geophys. Res. Oceans, sub judice.

Christensen-Dalsgaard, J (2002) Helioseismology. Rev. Mod. Phys. 74: 1073-1129.

Cramér, H (1940) On the theory of stationary random processes. Ann. Math. 41: 215-230.

Loève, M (1945) Sur les fonctions aléatoires stationnaires de second ordre. La Revue Scientifique 83: 297-303.

Mallows, CL (1967) Linear processes are nearly Gaussian. J. Appl. Prob. 4: 313-329.

Thomson, DJ, FL Vernon (2015) Unexpected, high-Q, low frequency peaks in seismic spectra. Geophys. J. Int. 202: 1690-1710.

Thomson, DJ, FL Vernon (2016) Some comments on the analysis of “big” scientific time series. Proc. IEEE 104: 2220-2248.

Thomson, DJ, LJ Lanzerotti, CG Maclennan (2001) The interplanetary magnetic field: Statistical properties and discrete modes. J Geophys. Res. 106: 15941-15962.

Thomson, DJ, LJ Lanzerotti, FL Vernon, MR Lessard, LTP Smith (2007). Solar modal structure of the engineering environment. Proc. IEEE 95: 1085-113.

# Wider broadband induction magnetometer development

V. Pronenko[1], T. Hanstein[2], M. Smirnov[2,3],

[1] LLC LEMI, Lviv, Ukraine, pron@isr.lviv.ua
[2] KMS Technologies-KJT Enterprises Inc., Houston, USA, Tilman@KMSTechnologies.com
[3] Luleå University of Technology, Sweden, maxim.smirnov@ltu.se

**ABSTRACT**

In broadband induction magnetometer (IM) design the compromise between intrinsic noise level in wide frequency band is optimized for the specific geophysical application on hand. Using a chopper amplifier gives us less noise at lower frequency (less than several hundred Hz) and using a voltage amplifier gives us less noise at higher frequency (more than 1 kHz). This means match of sensor and amplifier over a wide frequency band is contradictory to each other. An example is MFS-06 magnetometer which has 2 switchable bands. Here, we introduce a new design of broadband IM that operates in frequency from 0.1 mHz to 10 kHz. We concentrate on new ways and possibilities to find better matching between sensor and amplifier in a wider frequency band. Using modeling and experiments, we developed an optimum matched combination between possible magnetometer noise level and composite amplifier. Construction details and technical specifications of the broadband IM, LEMI-152, are presented.

For further demonstration of LEMI-152 magnetometer advantage, MT field tests with 2 sites were done at Hockley salt dome near Houston, Texas, USA. Site 1 is running with conventional broadband magnetometer LEMI-120 and the high frequency range has been acquired with LEMI-118 induction coils. Site 2 uses the new broadband magnetometer LEMI-152. The performance of the new magnetometer is verified by several parallel tests. For the MT data the magnetic time series are synchronized and the parallel components are compared. For the same coil type with the same coil response the difference of the two time series is taken and the power spectrum calculated. For different coil types with different response files, the difference is calculated in the complex Fourier domain after considering the calibration response for each magnetometer.

The data processing has been done with the new KMSpro-FastRobust processing software, which offers advanced parameter settings for optimized robust MT processing. The cultural noise in the test area is quite strong due to mining activity nearby, salt mine, gravel mine and Houston suburban within 500 m what complicated the processing. The sampling frequency ranges from 40 Hz to 80 kHz were applied. Different sampling frequency bands and a large variation processing parameters have been analyzed to optimize the noise filtering. Also different coherence criteria have been tested for rejection of bad data sequences. Transfer functions handle graphically and eliminate robust stacking bad parts of all different frequency bands. It gives the final transfer function, shown as apparent resistivity and phase and impedances. The obtained transfer functions are presented and compared.

**Keywords:** broadband induction magnetometer, MT, AMT, LEMI-152, magnetic sensors